



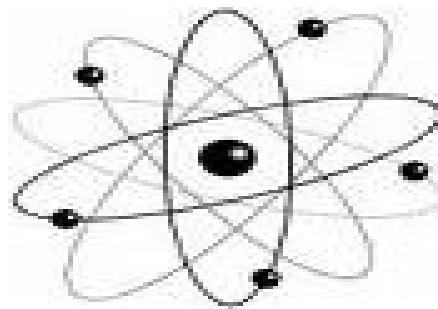
Democratic and Popular Republic of Algeria
Ministry of Higher Education and Scientific Research
University Med Khider of Biskra
Faculty of Exact Sciences and Nature and Life



Department of Matter Sciences

Domain of Matter Sciences

Section of Physics
Speciality Photovoltaic Physics



Final Dissertation in Master

Entitled:

**Simulation of Gallium Nitride (GaN) solar cell
by SILVACO-ATLAS**

Presented by:

NACEUR SOUFYANE

To the Jury composed by:

MEFTAH Amjad
SENGOUGA Nouredine
OUAHAB Abdelouahab

Professor
Professor
M.C. « A »

University Med Khider of Biskra
University Med Khider of Biskra
University Med Khider of Biskra

President
Reporter
Examiner

Academic Year
2013-2014

Abstract

Gallium Nitride (GaN) is used as an absorbent layer in multijunction cells. These solar cells are mainly used in space because they have a great resistance to cosmic radiation high-energy (MeV) thanks to the direct and wide energy gap. The only drawback in this solar cell is weak photo-current, which affects the overall current of the multijunction solar cell. In this work we study the effect of increasing the proportion of indium (In) which replaces Ga on the solar cell properties. The goal is to improve the photocurrent to be used in multijunction solar cells based on p-In_xGa_{1-x}N/n-In_xGa_{1-x}N junction. It was found that the proportion of indium (x = 0.78) gives a greater current (13.51 mA). However other parameters are degraded.

Keywords: Gallium Nitride, solar cell (pn), simulation (Silvaco/Atlas).

المخلص

تستخدم مادة نيتريد الغاليوم (GaN) كطبقة ماصة في مجال الخلايا الشمسية الفوتوفولطائية متعددة الوصلات. هذه الخلايا مستعملة أساسا في الفضاء لأنها تملك مقاومة كبيرة للإشعاعات الكونية (ذات طاقة عالية MeV) وذلك بفضل نطاقها الممنوع المباشر و الواسع. العيب الوحيد في هذه المادة هو التيار الضوئي الضعيف الذي يؤثر على التيار الكلي للخلية متعددة الوصلات في هذا العمل قمنا بدراسة تأثير زيادة نسبة الأنديموم (x) المعوضة للغاليوم على خصائص الخلية الشمسية المشكلة من الوصلة p-In_xGa_{1-x}N/n-In_xGa_{1-x}N. الهدف هو تحسين التيار الضوئي. لاستعماله في الخلايا متعددة الوصلات. لقد أظهرت نسبة الأنديموم (x=0.78) أكبر تيار (13.51 mA). بينما لوحظ تفهقر للخصائص الأخرى.

الكلمات المفتاحية: نيتريد الغاليوم ، الخلايا الشمسية (pn)، المحاكاة (سيلفاكو/أطلس).

Résumé

Le nitride de gallium (GaN) est utilisé comme couche absorbante dans des cellules à jonctions multiples. Ces cellules solaires sont principalement utilisées dans l'espace, car ils ont une grande résistance au rayonnement cosmique de haute énergie (MeV) grâce au gap d'énergie direct et large. Le seul inconvénient de cette cellule solaire est un faible photo-courant, ce qui affecte le courant global de la cellule solaire à jonctions multiples. Dans ce travail, nous étudions l'effet de l'augmentation de la proportion d'indium (In) qui remplace le Ga sur les propriétés des cellules solaires. L'objectif est d'améliorer le photocourant pour être utilisé dans des cellules solaires à jonctions multiples à base de la jonction p-In_xGa_{1-x}N/n-In_xGa_{1-x}N. On a trouvé que la proportion d'indium (x = 0,78) donne le maximum du photo-courant (13.51 mA). Cependant, les autres paramètres sont dégradés.

Mots clés: Nitrure de Gallium, cellules solaires (pn), simulation (Atlas/Silvaco).

SUMMARY

Summary :	
Acknowledgments	i
Abstract	ii
Summary	iii
General Introduction	vi
Chapter I: Properties of Gallium Nitride	1
I.1 Introduction	1
I.2 Crystallographic Properties	2
I.2.2 The structure of zincblende type cubic:	Erreur ! Signet non défini.
I.2.3 The structure NaCl type	2
I.3 Chemical properties of GaN	Erreur ! Signet non défini.
I.3.1 The surface chemistry of GaN	2
I.3.2 The stability of GaN at high temperature	3
I.4 Electrical properties of GaN	3
I.4.1 GaN mobilities	3
I.5 Optical properties of GaN	4
I.5 .1 Band gap energy of GaN	4
I.5.2 The temperature and pressure dependence of the GaN band gap	5
I.5.3 The optical constants of GaN	6
I.5.3.1 The refractive index of GaN	6
I.5.3.2 The absorption coefficient of GaN	7
I.5.3 .3 Emission properties of GaN	7
I.6. Properties of doped GaN	8
I.6.1 Mg doping	9
I.6.1 Cd Doping	9
I.6.3 Be Dopig	10
I.6.4 Hg Dopig	10
I.6.5 Group IV doping	10
I.6.6 Li doping	10
I.7 Growth techniques	10
I.7.1 Molecular beam epitaxy (MBE)	11

SUMMARY

I.7.2 Halide vapor phase epitaxy (HVPE)	11
I.7.3 Metal-organic chemical vapor deposition (MOCVD)	12
Chapter II: The Physics of solar cells	14
II.1 Introduction	14
II.2 Solar energy	14
II.2.1 The Sun	14
II.2.1.1 The structure of the Sun	15
II.2.1.2 Light	15
II.2.1.3 Waves	16
II.2.1.4 Absorption of light	16
II.2.2 Sunlight reaching earth	17
II.2.3 The impact of the movement of the earth on the solar radiation	19
II.2.4 Ground measurements of solar radiation	19
II.2.4.1 Pyrheliometer	19
II.2.4.2 Pyranometer	20
II.3 p-n Junctions	21
II.3.1 Structure and principle of operation	21
II.3.2 Flat band diagram	22
II.3.3 Thermal equilibrium	23
II.3.4 Forward and reverse bias	24
II.4 Physical processes in p-n junction of solar cells	25
II.4.1 Equivalent circuit of the solar cell	27
II.4.2 Solar cell parameters	28
II.4.2.1 Short circuit current (I_{sc})	29
II.4.2.2 Open circuit voltage (V_{oc})	29
II.4.2.3 Fill factor (FF)	29
II.4.2.4 Efficiency (η)	29
II.4.2.5 Series resistance (R_s)	30
II.4.2.6 Shunt resistance (R_{sh})	30
II.4.2.7 Quantum efficiency ($QE(\lambda)$)	30
II.4.3 Multijunction solar cell	30
II.4.3.1 Bandgap Selection	31

SUMMARY

II.5 Semiconductors	32
II.5.1 Band Theory of Solids	33
II.5.2 Recombination and generation	33
II.5.2.1 Band-to-band generation	34
II.5.2.2 Band-to-band recombination	34
II.5.2.3 R-G center recombination or indirect thermal recombination	34
II.5.3 Equilibrium carrier concentrations	35
Chapter III: The SILVACO ATLAS Simulator	38
III.1 Introduction	38
III.2 Silvaco Atlas Simulation Software	38
III.2.1 Atlas Inputs and Outputs	38
III.2.2 Using "Silvaco-Atlas" software	39
III.2.3 Running Atlas inside Deckbuild	40
III.2.4 Input file structure	40
III.3 Structure Specification	41
III.3.1 Mesh	41
III.3.2 Region	42
III.3.3 Electrodes	43
III.3.4 Doping	44
III.3.5 Materials Model Specification	44
III.3.5.1 Material	44
III.3.5.2 Models	45
III.3.5.3 Contact	45
III.3.5.4 Interface	45
III.3.6 Numerical Method Selection	46
III.3.7 Solution Specification	46
III.3.7.1 Log	46
III.3.7.2 Solve	47
III.3.7.3 Load and Save	47
III.3.8 Results Analysis	47
Chapter IV: Results and discussions	48
IV.1 Introduction	48
IV.2 Model description	4Erreur ! Signet non défini.

SUMMARY

IV.3 Simulation parameters	4 Erreur ! Signet non défini.
IV.4 Results and discussion	51
IV.4.1 Results for proportion of indium $x=0$ (GaN)	52
IV.4.2 Results for proportion of indium $x=0.20$ ($\text{In}_{0.2}\text{Ga}_{0.8}\text{N}$)	53
IV.4.3 Results for proportion of indium $x=0.39$ ($\text{In}_{0.39}\text{Ga}_{0.61}\text{N}$)	55
IV.4.4 Results for proportion of indium $x=0.52$ ($\text{In}_{0.52}\text{Ga}_{0.48}\text{N}$)	56
IV.4.5 Results for proportion of indium $x=0.57$ ($\text{In}_{0.57}\text{Ga}_{0.43}\text{N}$)	57
IV.4.6 Results for proportion of indium $x=0.65$ ($\text{In}_{0.65}\text{Ga}_{0.35}\text{N}$)	59
IV.4.7 Results for proportion of indium $x=0.68$ ($\text{In}_{0.68}\text{Ga}_{0.32}\text{N}$)	60
IV.4.8 Results for proportion of indium $x=0.78$ ($\text{In}_{0.78}\text{Ga}_{0.22}\text{N}$)	62
IV.4.9 Results for proportion of indium $x=0.84$ ($\text{In}_{0.84}\text{Ga}_{0.16}\text{N}$)	63
IV.4.10 Results for proportion of indium $x=0.89$ ($\text{In}_{0.89}\text{Ga}_{0.11}\text{N}$)	65
IV.4.11 Results for proportion of indium $x=[0-0.89]$	66
IV.5 Summary of indium content in the InGaN (x) absorber layer effect	67
IV.5 .1 The effect on the short circuit current	67
IV.5 .2 The effect on the open-circuit voltage V_{oc}	67
IV.5 .3 The effect on the fill factor (FF)	68
IV.5 .4 The effect on the efficiency	69
IV.6 Comparison between best results of p-n and n-p at $x=0.84$, $\text{In}_{84}\text{Ga}_{16}\text{N}$	69
Chapter V: General Conclusion	71
General Conclusion	71
REFERENCES	72

GENERAL INTRODUCTIN

Nitride-based materials such as $\text{In}_x\text{Ga}_{1-x}\text{N}$ have become important in fabricating photovoltaic devices due to their band gap energies lying between 0.7 and 3.4 eV [1–2]. It can absorb the full solar spectrum by a single material of $\text{In}_x\text{Ga}_{1-x}\text{N}$ with different indium contents. Many theoretical calculations on the performance evaluation of InGaN-based solar cells have been performed [1-3]. They demonstrated that a very high solar efficiency could be achieved. The direct bandgap properties and high absorption coefficients make it have great potential in photovoltaic application. Further, the GaN-based materials have a high resistant to high energy irradiation and temperature variations [5, 6]. Thus, it is suitable for space applications or high concentrator solar cell systems. However, a good-quality InGaN film with high indium composition cannot be obtained due to the low miscibility of InN in GaN.

The goal of our work is to study the effect of the proportion of indium of the GaN absorber layer on the density of current in p- InGaN/ n-InGaN solar cell. For this we have used numerical simulation to study this effect. The numerical simulation is based on the SILVACO TCAD software.

This memory is organized in a general introduction, four chapters and a conclusion. In the introduction the importance of the work is briefly outlined. In the first chapter, we introduced the GaN material. In particular its chemical, crystalline and optical properties are detailed. In the second chapter, we present the solar radiation. The operation of the p-n junction and the solar cell are also discussed. The third chapter is dedicated to give a detailed description on the software (SILVACO TCAD) used for the stimulation of our device. Finally, the fourth chapter presents and discusses the numerical results obtained of the simulation of a p- $\text{In}_x\text{Ga}_{1-x}\text{N}$ /n- $\text{In}_x\text{Ga}_{1-x}\text{N}$ solar cell. The work finished with a conclusion which summarizes the realized work.

Chapter I

Properties of Gallium Nitride

I.1 Introduction

As all other III-nitrides Gallium Nitride (GaN) has partially covalent and partially ionic bonds. The ionic bond is relatively higher that explains the significant hardness and chemical stability of GaN. Other superior material properties such as high electron mobility, high thermal conductivity, and high critical field combined with direct wide band gap make GaN attractive for many electronic and optoelectronic applications.

I.2 Crystallographic Properties

GaN crystallizes in two different forms at room temperature: the hexagonal or würtzite structure and cubic structure or zinblende (sphalerite) (ZnS). The morphological forms of GaN crystals of the hexagonal structure is shown in Figure I.1.

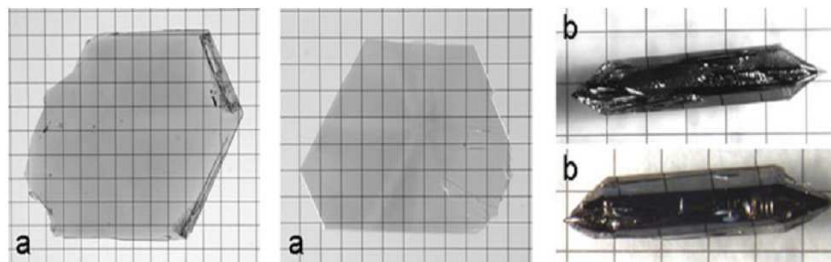


Figure I.1: Two morphological forms of GaN crystals: (a) Hexagonal platelets et (b) Hexagonal needles. Grid: 1mm

At high pressure, it adopts a NaCl-type structure. These different structures are shown in Figure I.2.

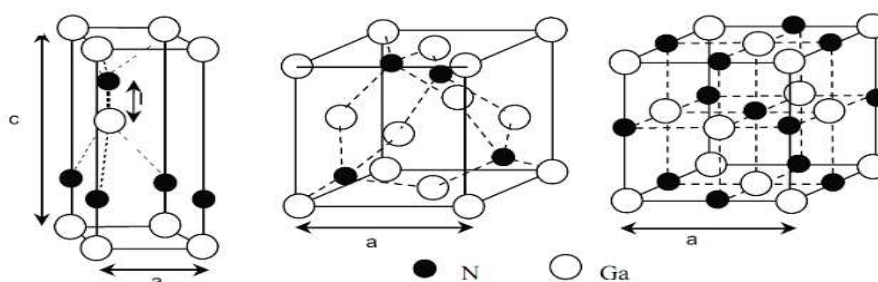


Figure I.2: The crystalline structures of GaN: (a) würtzite, (b) Zinblende and (c) NaCl.

I.2.1 The hexagonal wurtzite structure

This structure is also known as α -GaN. It is a very thermodynamically stable structure, constituted by two compact hexagonal subnets, one containing the gallium atoms (Ga) and the other nitrogen atoms (N), and interpenetrating offset along the axis of $\frac{5}{8}$ th of the unit cell. This structure is characterized by the lattice parameters a and c . In reciprocal space, the first Brillouin zone has a hexagonal section.

I.2.2 The structure of zincblende type cubic

This structure is also known as β -GaN. Thermodynamically metastable, it consists of two subnetworks: face centered cubic gallium atoms and nitrogen offset by one fourth of the diagonal of the mesh. The reciprocal of this network structure is a face-truncated octahedron.

I.2.3 The structure NaCl type

This is the high-pressure wurtzite structure variety, the transition between the two structures occurs around 50 GPa. It is composed of two subface centered cubic lattices of atoms of gallium and nitrogen, shifted by $a/2$.

I.3 Chemical properties of GaN

GaN was first synthesized by Johnson et al [7] in 1928 who noted that "Gallic nitride is an exceedingly stable compound". It is this chemical stability at elevated temperatures combined with its wide band gap that has made GaN an attractive material for device operation in high temperature and caustic environments. GaN is also an excellent candidate for protective coatings due to its hardness. However, the majority of GaN research is interested in semiconductor device applications. While the thermal stability of GaN should allow high temperature processing steps to be performed, the chemical stability of GaN presents a technological challenge. There have been many reports describing the resistance of GaN films to the conventional wet etching techniques used in semiconductor processing.

I.3.1 The surface chemistry of GaN

Several groups have studied the surface chemistry of GaN using the techniques of Auger electron spectroscopy (AES) [8], x-ray photoemission spectroscopy (XPS) [9], and electron energy-loss spectroscopy (EELS) [8]. There were also a number of studies examining

the thermal stability and dissociation of GaN. However, the material studied was generally not well characterized and the results from different laboratories varied widely.

I.3.2 The stability of GaN at high temperature

Studied the stability of GaN at high temperature, significant weight losses were reported at temperatures as low as 750 °C by Furtado and Jacob [10] while no significant losses were observed at 1000 °C by Morimoto [11].

Observed that GaN was less stable in a HCl or H₂ atmosphere while the best results were obtained in N₂ [10]. Some controversy exists over the reaction which dominates the decomposition of GaN. Munir and Searcy [12] measured the apparent vapor pressure of GaN and calculated the heat of sublimation to be 72.4 ± 0.5 kcal/mol.

I.4 Electrical properties of GaN

Control of the electrical properties of GaN remains the foremost obstacle hindering device efforts. Unintentionally doped GaN has in all cases been observed to be n type with the best samples still showing an electron concentration $n \sim 4 \times 10^{16}/\text{cm}^3$ [8]. No impurity has been shown to be present in sufficient quantity to account for the carriers, so researchers have attributed the background to native defects which are widely thought to be nitrogen vacancies. All efforts, until recently, to obtain p-type doping have resulted in heavily compensated, highly resistive films. The development of a reliable p-type doping technique for GaN remains a primary challenge for researchers.

I.4.1 GaN mobilities

Nakamura [13] has reported acceptable GaN mobilities in 1991. Room-temperature and liquid nitrogen temperature mobilities of $\mu_n \sim 600 \text{ cm}^2/\text{V}$ and $\mu_n \sim 1500 \text{ cm}^2/\text{V}$ at carrier concentrations of $n = 4 \times 10^{16}/\text{cm}^3$ and $n = 8 \times 10^{15}/\text{cm}^3$ were measured. Ilegems and Montgomery [14] performed temperature dependent Hall measurements from 10-900 K on GaN having a room-temperature background electron concentration $n = 3 \times 10^{17}/\text{cm}^3$ and a room-temperature mobility of $\mu_n \sim 300 \text{ cm}^2/\text{Vs}$. Their data are shown in Figure I.3. In their best layer, the mobility peaked at $\mu_n \sim 800 \text{ cm}^2/\text{Vs}$ at 150 K and decreased at lower temperatures which the authors attributed to the onset of impurity band conduction. In the 300-900 K range, the mobility tended to vary with T^{-2} , and at 900 K, a mobility of $\mu_n \sim 25 \text{ cm}^2/\text{Vs}$ was measured.

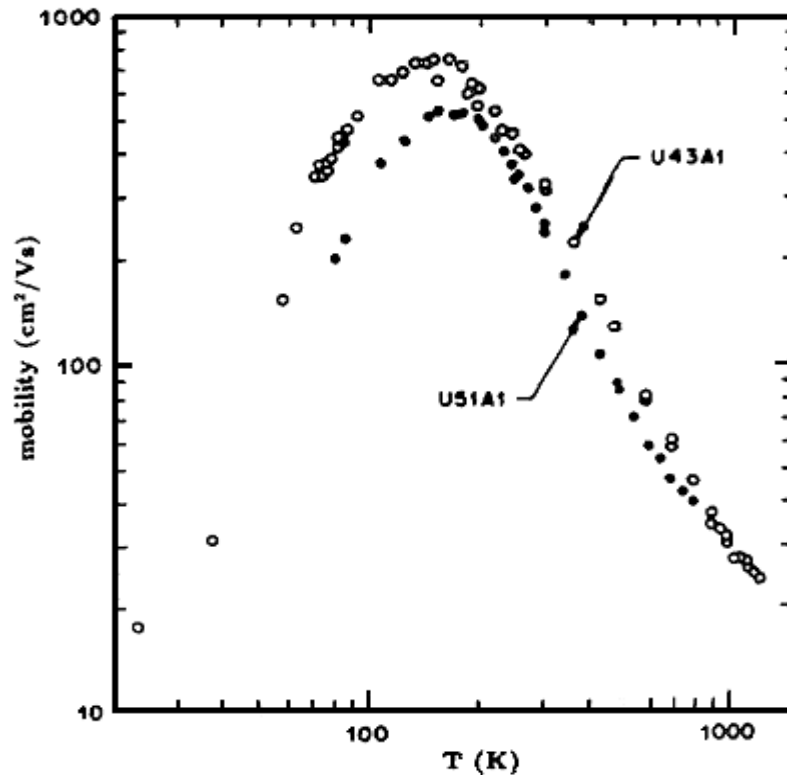


Figure I.3: Temperature dependence of the electron mobility in unintentionally doped GaN having room-temperature background electron concentrations (U43A1) $n=2 \times 10^{17}/\text{cm}^3$ and (U51A1) $n=4 \times 10^{17}/\text{cm}^3$ [14].

I.5 Optical properties of GaN

GaN is primarily of interest for its potential as a blue and UV light emitter. For that reason, much of the effort devoted to GaN has been directed towards determining its optical properties. A fairly complete account of the optical properties of wurtzite GaN is possible.

I.5.1 Band gap energy of GaN

Maruska and Tietjen [15] were the first to accurately measure the GaN direct band gap energy to be 3.39 eV (Figure I.4). Soon after, Pankove et al [16] reported a low temperature (1.6 K) GaN PL spectrum. Strong near gap emission was observed at 3.477 eV and a weaker peak was noted at 3.37 eV which split into a ~10 meV spaced doublet when the temperature was increased to 35 K. The separation of the two bands was taken to represent a lower bound of the donor binding energy. Using a value of $\epsilon_0 = 9.8$ obtained from the GaN phonon energies, and a donor binding energy of 42 ± 1 meV, an electron effective mass $m^* = 0.25m_0$ was calculated. An acceptor binding energy of ~200

meV was also estimated. At 300 K the energy of the highest energy transition had decreased to 3.39 eV which is in excellent agreement with the observations of Maruska and Tietjen [16].

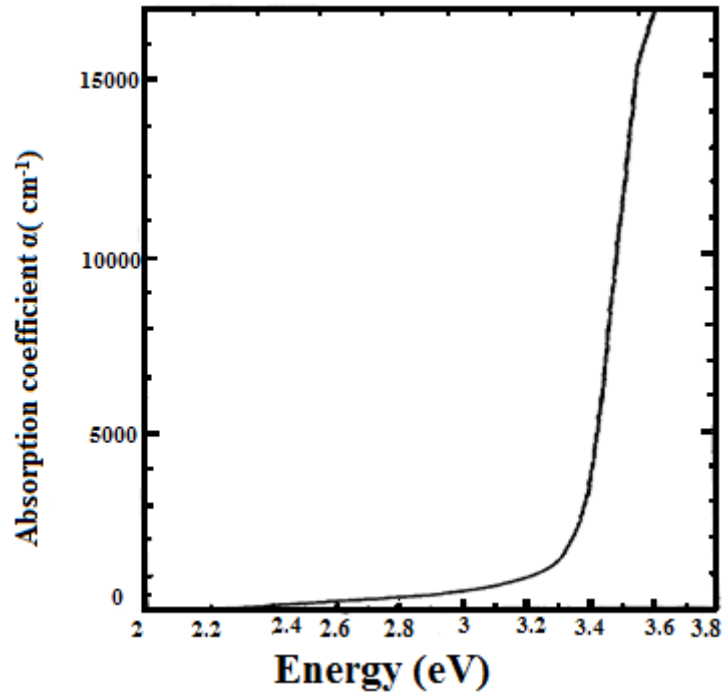


Figure I.4: Room-temperature absorption spectrum of GaN [11].

I.5.2 The temperature and pressure dependence of the GaN bandgap

Several groups have measured the temperature dependence of the GaN bandgap. Pankove et al [16] estimated a bandgap temperature coefficient of $dE_g/(dT) = -6.0 \times 10^{-4} \text{ eV/K}$ in the linear region above 180 °C from the temperature dependence of the principle emission peak. Monemar [17] determined the fundamental bandgap to be $3.503 \pm 0.0005 \text{ eV}$ at 1.6 K and fitted the temperature dependence of the bandgap to the empirical relation:

$$E_g = 3.503 + (5.08 \times 10^{-4} T^2) / (T - 996) \text{ eV} \quad (\text{I.1})$$

Optical transmission measurements were also used to study its evolution as a function of pressure [18]:

$$E_g = E_g(P=0) + 0.47.P + 0.0018.P^2 \text{ eV} \quad (\text{I.2})$$

Camphausen and Connell [19] studied the pressure and temperature dependence of the GaN absorption edge. Under hydrostatic pressure up to 10 kbar, the GaN bandgap energy shifted by $dE_g/(dP) = 4.2 \pm 0.4 \text{ meV/kbar}$ at room temperature. The temperature dependence was measured to be $dE_g/(dT) = -6.7 \times 10^{-4} \text{ eV/K}$.

I.5.3 The optical constants of GaN

In these studies. Although there have been many reports on the optical properties and constants of GaN, the current state of the available data is seemed to be less than adequate. In particular, the optical constants.

I.5.3.1 Therefractiveindexof GaN

There have been several measurements of the optical constants of GaN. Ejder [20] measured the refractive index of GaN using transmission and absorption measurements and obtained values of $n(3.38\text{eV}) = 2.67$ and $n(1.0\text{eV}) = 2.33$.

In the particular case where the material is isotropic, the complex refractive index is written as follows:

$$\mathbf{N} = \mathbf{n} + \mathbf{iK} \quad (\mathbf{I.3})$$

where n is the real part of the refractive index and K is the extinction coefficient.

The complex index is related to the dielectric constant by the relationship:

$$\epsilon_r = \mathbf{N}^2 = \mathbf{n}^2 - \mathbf{K}^2 + 2\mathbf{i}n\mathbf{K} \quad (\mathbf{I.4})$$

$$\text{such as: } \epsilon_r = \epsilon_1 + \mathbf{i}\epsilon_2 \quad (\mathbf{I.5})$$

$$\text{It comes: } \epsilon_1 = \mathbf{n}^2 - \mathbf{K}^2 \text{ and } \epsilon_2 = 2\mathbf{nK} \quad (\mathbf{I.6})$$

In the range of transparency away from the gap energy of the semiconductor band, the variation of the real index of refraction as a function of the wavelength is given by the Sellmeier law [21]:

$$n(\lambda) = \sqrt{a + \frac{b\lambda^2}{\lambda^2 - c^2}} \quad (\mathbf{I.7})$$

a , b and c are the Sellmeier coefficients. This is shown in Figure I.5.

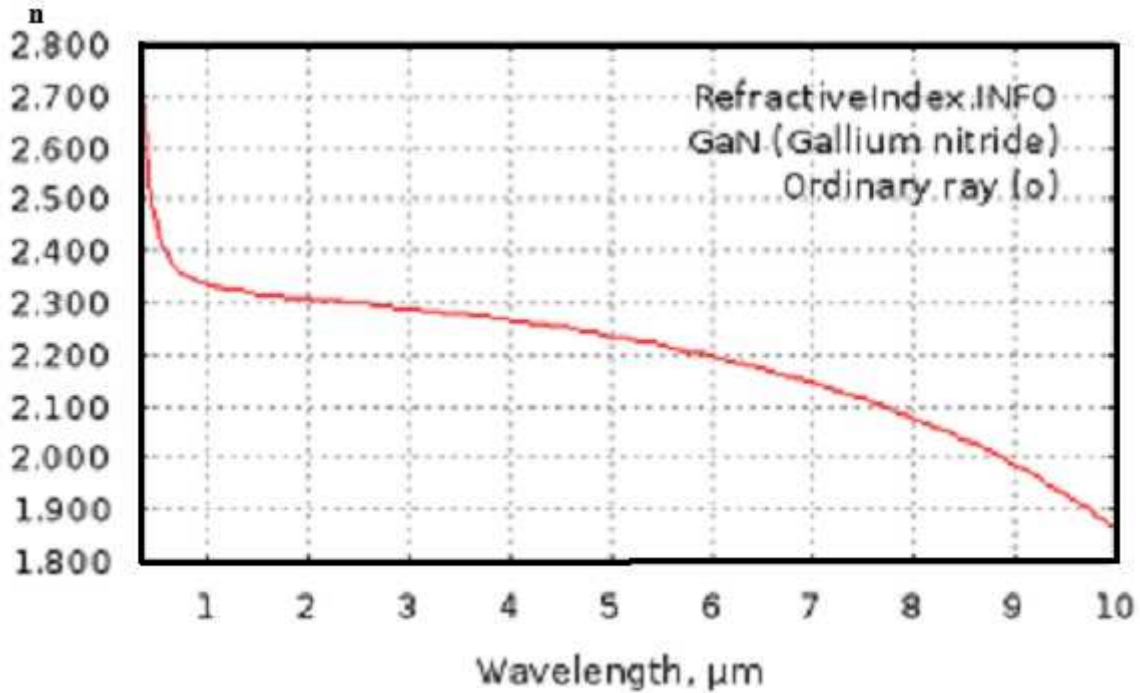


Figure I.5: Refractive index of GaN between 0.35 and 10 μm wavelength.

I.5.3.2 The absorption coefficient of GaN

The absorption coefficient has also been the subject of several studies. For materials with a direct gap, the value of the square of the coefficient is linear with the energy of photons above the energy gap, that is:

$$\alpha^2 = (\alpha_0)^2 (E - E_g) \quad (\text{I.8})$$

This coefficient is related to the extinction coefficient by the following equation:

$$\alpha = \frac{4\pi\nu}{c} K \quad (\text{I.9})$$

c and ν are respectively the speed and frequency of the light.

I.5.3.3 Emission properties of GaN

Stimulated emission has been achieved in GaN by optical pumping in a number of laboratories. Dingle et al [22] were the first to report lasing in GaN. Their single crystal GaN needles emitted at a photon energy of $\sim 3.45 \text{ eV}$ at 2K. Catalano et al [13] was able to observe 80K stimulated emission in GaN at 3.435 eV with an optical gain of $\sim 10^3 \text{ cm}^{-1}$. Amano et al [23] observed stimulated emission at room temperature for the first time. Khan et al [24] has since reported room-temperature stimulated emission in GaN from a vertical (c-oriented) cavity. A summary of the structural, optical, properties of Würtzite GaN is presented in Table 1.1.

Table I.1: Properties of würtzite GaN

GaN	Parameter value	References
Band gap energy	$E_g(300\text{ K}) = 3.39\text{ eV}$	[16]
	$E_g(1.6\text{ K}) = 3.50\text{ eV}$	[18]
Band gap temperature coefficient ($T > 180\text{ K}$)	$\Delta E_g / (dT) = -6.0 \times 10^{-3}\text{ eV/k}$	[17]
Band gap pressure coefficient ($T = 300\text{ K}$)	$\Delta E_g / (dP) = 4.2 \times 10^{-3}\text{ eV/kbar}$	[26]
Lattice constant ($T = 300\text{ K}$)	$a = 3.18910^{-10}\text{ m}$	[16]
	$c = 5.18510^{-10}\text{ m}$	
Coefficient of thermal expansion ($T = 300\text{ K}$)	$\Delta a / a = 5.59 \times 10^{-6}\text{ K}^{-1}$	[16]
	$\Delta c / a = 3.17 \times 10^{-6}\text{ K}^{-1}$	
Thermal conductivity	$K = 1.3\text{ W/cm K}$	[27]
Index of refraction	$n(1\text{ eV}) = 2.33$	[21]
	$n(3.38\text{ eV}) = 2.67$	
Electron effective mass	$m_e^* = 0.20 \pm 0.02 m_0$	[28]

I.6. Properties of doped GaN

There has been much effort aimed at doping p type GaN by introducing group II and IV elements. Many potential dopants have been incorporated into GaN and their optical properties, shown schematically

in Figure I.6. Some impurities have been observed to effectively compensate electrons in GaN leading to highly resistive material.

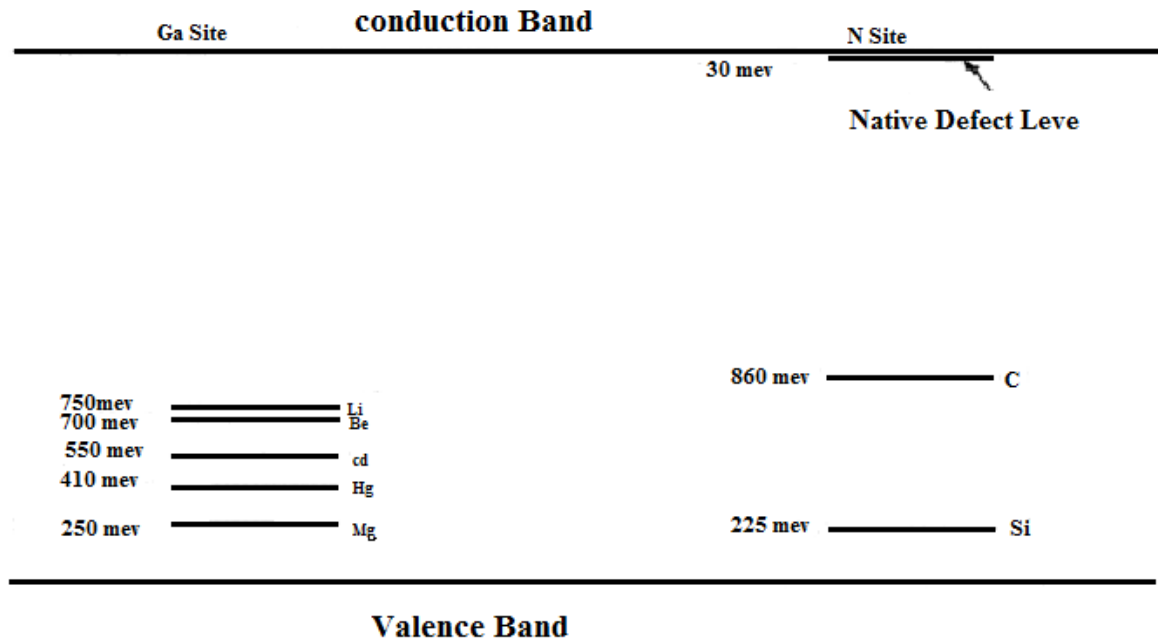


Figure I.6: Estimated ionisation energies of some substitutional acceptors in GaN. Also shown is the shallow donor level, generally thought to be the nitrogen vacancy, which is responsible for the n-type background carrier concentration observed in GaN [17].

I.6.1 Mg doping

Akasaki and co-workers [28] developed a technique which converts Mg-compensated GaN into p-type material as a result of electron beam irradiation. Nakamura et al [29] has succeeded in growing p-type GaN by metalorganic CVD (MOCVD) which had a hole concentration $p = 2 \times 10^{15} / \text{cm}^3$. Optical measurements have shown that the acceptor levels in GaN are several hundred milli-electronvolts above the valence band edge. In order to grow GaN which has significant p-type conductivity at room temperature, existing Mg-doping methods must be improved or acceptor complexes which lie close to the valence band edge must be sought.

I.6.2 Cd Doping

There have been several reports which describe attempts to dope GaN with Cd. Bergman et al [30], were able to dope GaN with a small amount of Cd, but a sufficient amount to compensate the electron background concentration could not be incorporated. Ilegemsetal [31] reported the Cd-related peak at 2.85 eV. Bergman et al [30], measured a $1 \mu\text{s}$ decay time at 77K for their 2.7 eV emission.

I.6.3 Be Doping

Two groups reported Be-doped GaN. Be was observed to effectively compensate the free electrons and high resistivity GaN was obtained. Optical measurements detected a broad Be-related emission at an energy of ~ 2.2 eV.

I.6.4 Hg Doping

Two groups have investigated Hg doping. No electrical measurements were reported. Pankove and Hutchby [32] observed 2.43 eV emission in Hg-doped samples. Ejder and Grimmeiss [33] observed 2.9 eV emission and estimated the Hg-acceptor level to be 410 meV above the valence band.

I.6.5 Group IV doping

Group IV elements have been investigated as possible p-type dopants in the hope that they would occupy vacant nitrogen sites in GaN. Cunningham et al [34] observed an order of magnitude reduction in the free carrier concentration when Ge doping was attempted. Maruska and Tietjen [15] reported occasional p-type conduction in Ge-doped GaN, but later retracted this claim [13]. In the same work, Si was observed to markedly reduce the electron concentration in GaN to as little as $n = 3 \times 10^{16}/\text{cm}^3$ but p-type conductivity was not achieved.

I.6.6 Li doping

A number of workers have investigated Li doping. Pankove et al [35] obtained compensated GaN using Li doping. The Li acceptor luminescence was observed at 2.23 eV. Ejder and Grimmeiss [33] estimated the Li-acceptor level to be 750 meV above the valence band.

I.7 Growth techniques

When heated at atmospheric pressure GaN dissociates rather than melts, thus growth from liquid solution at reasonable conditions is impossible as it mentioned above. Therefore vapor phase deposition techniques are used for GaN synthesis; three major methods exist nowadays, MBE, HVPE and MOCVD, which will be described in more detail.

I.7.1 Molecular beam epitaxy (MBE)

MBE is a non-equilibrium vapor phase epitaxy growth method where solid or gas source elements are heated in evaporators, known as Knudsen effusion cells, to produce beams of atoms impinging on the substrate, which is rotated and heated to appropriate temperatures. The effused atoms need to have mean free paths bigger than the size of the chamber, also to obtain films of sufficient purity low levels of residual gases must be sustained, therefore ultra-high vacuum (10^{-9} Torr) is needed, which is the drawback of this method. The advantages are the lower, compared to other methods, growth temperatures of 600 – 800 °C and possibility to grow very thin layers with fine control of composition. Precision of this growth technique is based on low deposition rates and in-situ characterization capabilities. For example, reflection high energy electron diffraction (RHEED) detector allows to control the thickness of the film up to one atomic monolayer.

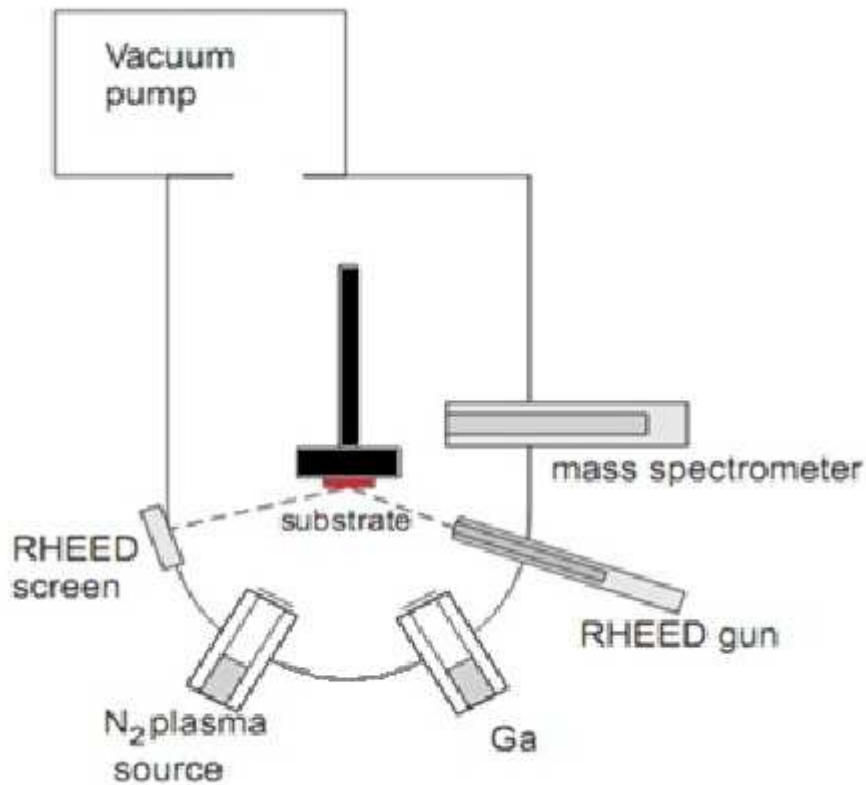


Figure I.7: Schematic drawing of MBE chamber for GaN growth.

I.7.2 Halide vapor phase epitaxy (HVPE)

A typical horizontal hot wall HVPE reactor is depicted on Figure I.8. The chamber is made of quartz and can be heated resistively or by RF induction. There are two temperature zones. The

metallic source zone is kept at the temperature of ~ 800-900 °C, which is lower than the growth zone temperature (1000-1100°C).

By using several temperature zones more flexibility in controlling and in adjusting growth conditions can be achieved.

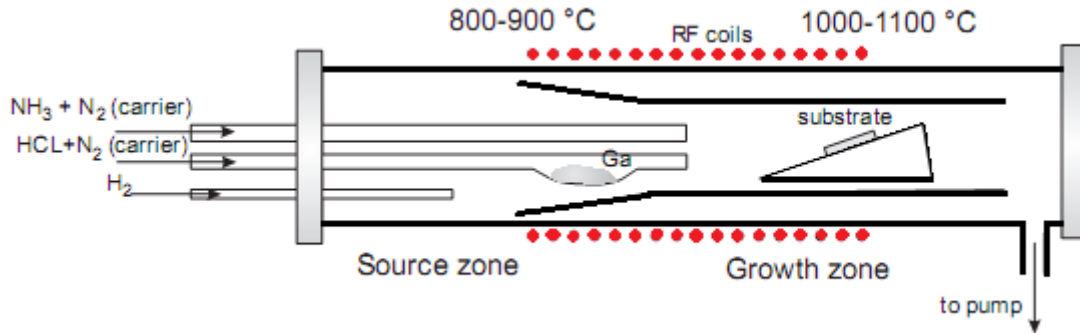


Figure I.8: Schematic drawing of HVPE growth reactor.

Hydrogen chloride is let into the quartz tube with melted Ga where the reaction producing gallium chloride occurs:



The efficiency of this process is very high, above 95%. In a separate tube NH_3 , the group V source, is flowed. Subsequently ammonia and gallium chloride undergo the following reaction on the surface of the substrate:



To prevent parasitic growth in the gas inlet ammonia and halide (GaCl) should not be mixed before they reach the substrate. Light molecule gases such as H_2 or mixtures of N_2 and H_2 are used as carrier gases to obtain laminar flow. The deposition rate is ~ 100- 300 $\mu\text{m/h}$ and is very high compared to MBE, which is why HVPE is commercially used for growing thick GaN layers. The process occurs at atmospheric pressure, at near equilibrium conditions and is mass transport limited by the flow of halide precursor.

I.7.3 Metal-organic chemical vapor deposition (MOCVD)

MOCVD is a technique similar to HVPE, only instead of inorganic species metal-organic precursors are flown in the reactor as sources of Ga. Specifically trimethyl-gallium ($(\text{CH}_3)_3\text{Ga}$) is used as Ga, and ammonia—as nitrogen precursors. Organic species and ammonia are transported in separate pipes to the quartz chamber to prevent premature reacting. Lighter carrier gases (H_2 or N_2) are let through organic compound liquids thus transporting the precursors to the reactor.

These compounds are thermally dissociated over the surface of $\sim 1000^\circ\text{C}$ hot substrate and react in a sequence of complex reactions forming GaN. In hot wall MOCVD the whole reactor is heated by RF coils, whereas in the cold-wall process only the susceptor, which is usually made of graphite, is heated. The substrate may be rotated to obtain uniform films. Before the growth is started nitridation of the substrate is usually done to reduce lattice mismatch due to the nitrides formed on the substrate surface (SiN on SiC or AlN on Al_2O_3). The usual practice is to start epitaxial growth on sapphire substrates with a low-temperature ($\sim 600^\circ\text{C}$) GaN buffer layer. Ease of scalability, high uniformity and quality of the films, and a relatively high growth rates ($\sim 1\mu\text{m/h}$) are making this technique the method of choice for commercial purposes.

Chapter II

The Physics of solar cells

II.1 Introduction

Semiconductor solar cells are fundamentally quite simple devices. Semiconductors have the capacity to absorb light and to deliver a portion of the energy of the absorbed photons to carriers of electrical current – electrons and holes. A semiconductor diode separates and collects the carriers and conducts the generated electrical current preferentially in a specific direction. Thus, a solar cell is simply a semiconductor diode that has been carefully designed and constructed to efficiently absorb and convert light energy from the sun into electrical energy.

II.2 Solar energy

The sun is responsible for nearly all of the energy available on earth. The exceptions are attributable to moon-tides, radioactive material, and the earth's residual internal heat. Everything else is a converted form of the sun's energy: Hydropower is made possible by evaporation-transpiration due to solar radiant heat, the winds are caused by the sun's uneven heating of the earth's atmosphere, fossil fuels are remnants of organic life previously nourished by the sun; and photovoltaic electricity is produced directly from sun-light by converting the energy in sunlight into free charged particles within certain kinds of materials.

Solar energy can be used to produce electricity by converting solar radiation directly into an electric current through the so-called solar cells or photovoltaic cells. The electrical power produced can either be injected directly into the grid (grid connected) or used in-situ (off-grid).

II.2.1 The Sun

Schematic structure of the Sun is shown in Figure II.1. The Sun's energy is the result of several nuclear fusion reactions, the main being the process in which hydrogen (four protons) merges and forms helium. The mass of alpha particle (helium nucleus) is less than the mass of four protons, the difference in mass is converted into energy according to Einstein's formula

$$E = mc^2 \quad (\text{II.1})$$

II.2.1.1 The structure of the Sun

The Sun is a large sphere of intensely hot gases consisting, by mass, about 75 % of hydrogen, 23 % of helium and others (2 %). This proportion changes slowly over time referring to the nuclear fusion in its core with temperatures of approximately 15 - 20 million K. Hydrogen atoms fuse there to form helium and this energy is then delivered as radiation (light and heat) into space. The Sun's outer surface, namely photosphere, has an effective blackbody temperature of approx. 6000 K. This mean, as viewed from the Earth, the radiation emitted from the Sun appears to be essentially equivalent to that emitted from a blackbody at 6000 K [37]. To understand the behaviour of the radiation from the Sun the characteristics of the blackbody should be discussed here.

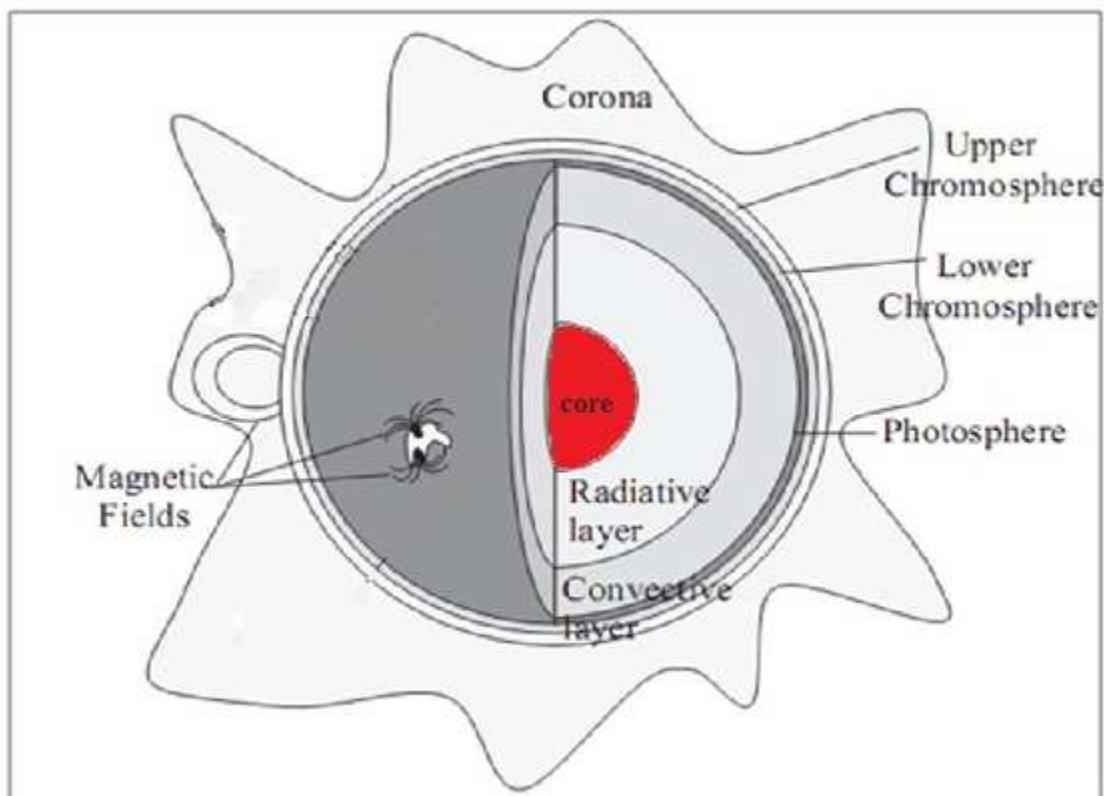


Figure II.1: The structure of the Sun.

II.2.1.2 Light

The Earth receives energy from the Sun by way of radiated energy. This radiated energy is carried by tiny particles having no mass called photons. Photons behave like waves and, as such, have a characteristic wavelength, frequency, and energy. It is the energy of these photons that is used in photovoltaic cells to excite electrons so that an electrical current can be produced.

II.2.1.3 Waves

Figure II.2 illustrates that the wavelength of a wave is the distance between two successive peaks, or maxima, of a wave.

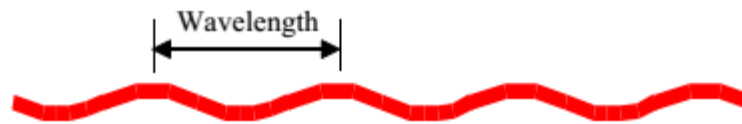


Figure II.2: Wavelength of wave.

The frequency of a wave is a measure of how many peaks are observed in one second from a stationary point along a wave's path. The product of the wavelength and frequency gives the wave's velocity:

$$v = \lambda f \quad (\text{II.2})$$

All radiative, or light, energy travels at the same velocity, commonly known as the speed of light, which is about $300,000,000 \text{ m/s}$ ($3 \times 10^8 \text{ m/s}$). Because the velocity of light is a constant and also a product of frequency and wavelength, specific frequencies of light are associated with specific wavelengths.

II.2.1.4 Absorption of light

Photons incident on the surface of a semiconductor will be either reflected from the top surface, will be absorbed in the material or, failing either of the above two processes, will be transmitted through the material. For photovoltaic devices, reflection and transmission are typically considered loss mechanisms as photons which are not absorbed do not generate power. If the photon is absorbed it has the possibility of exciting an electron from the valence band to the conduction band. A key factor in determining if a photon is absorbed or transmitted is the energy of the photon. Therefore, only if the photon has enough energy will the electron be excited into the conduction band from the valence band. Photons falling onto a semiconductor material can be divided into three groups based on their energy compared to that of the semiconductor band gap:

$E_{ph} < E_G$ Photons with energy E_{ph} less than the band gap energy E_G interact only weakly with the semiconductor, passing through it as if it were transparent.

$E_{ph} = E_G$ have just enough energy to create an electron hole pair and are efficiently absorbed.

$E_{ph} > E_G$ Photons with energy much greater than the band gap are strongly absorbed. However, for photovoltaic applications, the photon energy greater than the bandgap is wasted as electrons quickly thermalize back down to the conduction band edges.

II.2.2 Sunlight reaching earth

Even though the sun ranks as a run-of-the-mill star, it releases a huge quantity of energy in terms of human capacity or need. Power output per second is 3.86×10^{20} megawatts (MW). This energy fills the solar system, bathing the earth's atmosphere with a near constant supply of 1.37 kilowatts per square meter (kW/m^2). Not all of the direct sunlight incident on earth's atmosphere arrives at the earth's surface. The atmosphere attenuates many parts of the spectrum (Figure II.3). For example, X-rays are almost totally absorbed before reaching the ground. A good percentage of ultraviolet radiation is also filtered out by the atmosphere. Some radiation is reflected back into space. Some is randomly scattered by the atmosphere, which makes the sky look blue.

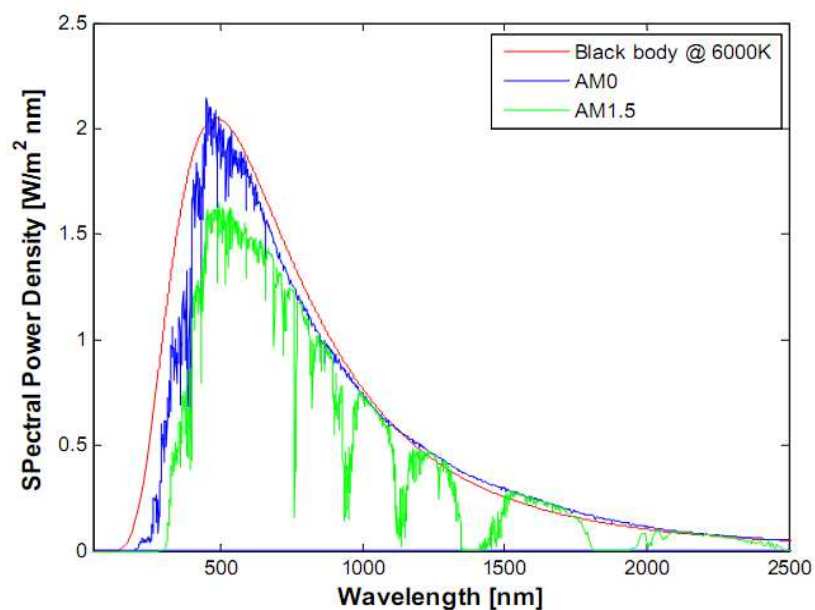


Figure II.3: Spectral power density of black-body radiation at 6000 K, AM0 and AM1.5 spectra.

It is valuable to relate the amount of sunlight at the earth's surface to the quantity, or air mass (AM), of atmosphere through which the light must pass. Radiation arriving at the surface of the earth is measured against that reaching the fringes of the atmosphere, where there is no air, and the air mass is zero (AM0). The light of the high-noon sun (and under further specified conditions) passes through an air mass of one (AM1). The intensity of the sunlight reaching the ground weakens for sun angles approaching the horizon since the rays have more atmosphere, or

air mass, to penetrate. The atmosphere is a powerful absorber and can cut the sun's energy reaching the earth by 50% and more.

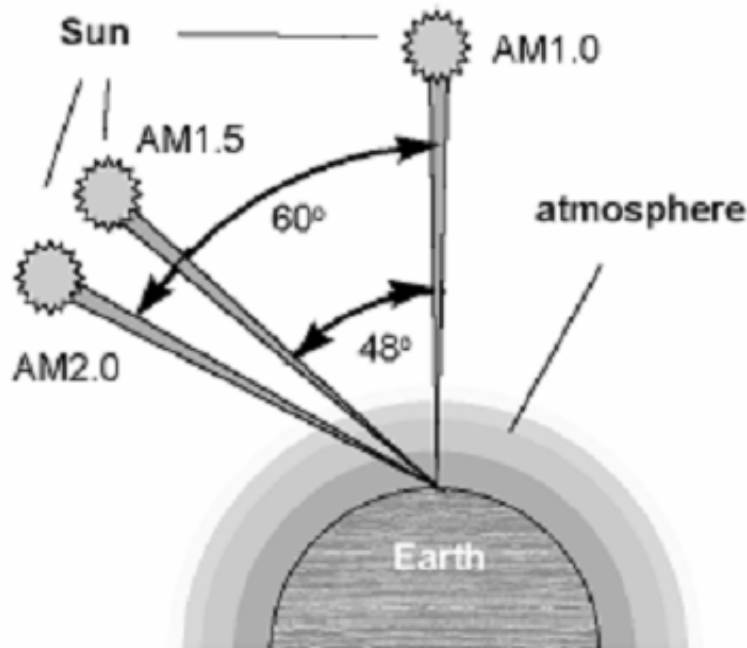


Figure II.4: The Path length (in unit of air mass) changes with the zenith angle.

The Earth revolves in orbit around the Sun, that is approximately circular circumference deviation does not exceed 1.7%. The average distance between the Sun and the Earth (Figure II.5), called the astronomical unit is equal to 1,495 1011 m. The Sun, as viewed from the Earth's surface, represents a disk with an angular diameter 32'

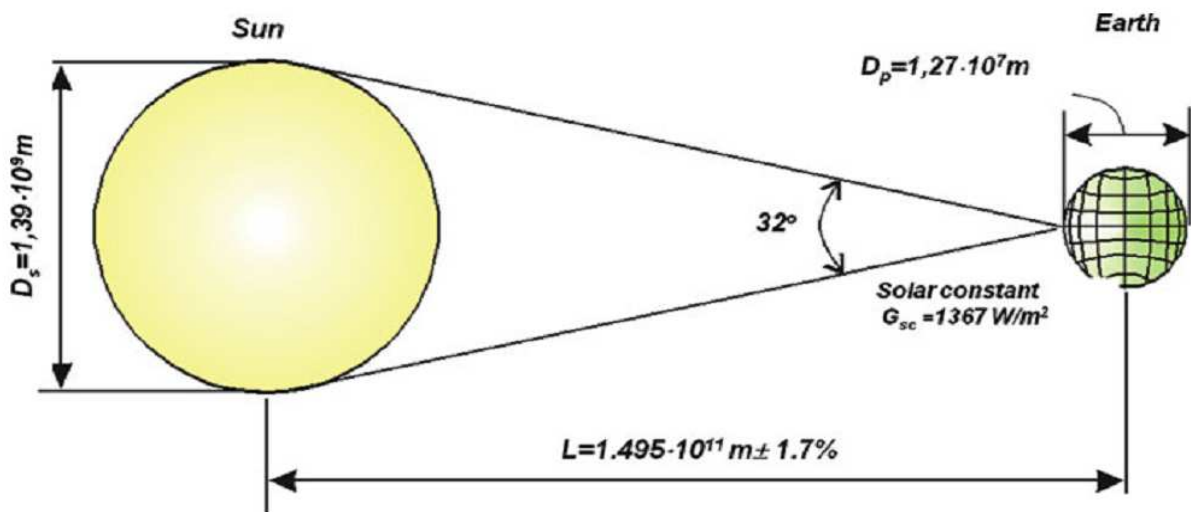


Figure II.5: Geometry of the (Sun-Earth) system.

II.2.3 The impact of the movement of the earth on the solar radiation

The Earth rotates in an elliptical orbit around the Sun during 1 year with the Sun in one of the focal points. Also, the Earth rotates around its axis, making one revolution in 24 h. The Earth's axis of rotation has a fixed direction in space and is inclined at angle $\delta_0 = 23.44^\circ$ towards the normal line in the orbit plane (Figure II.6).

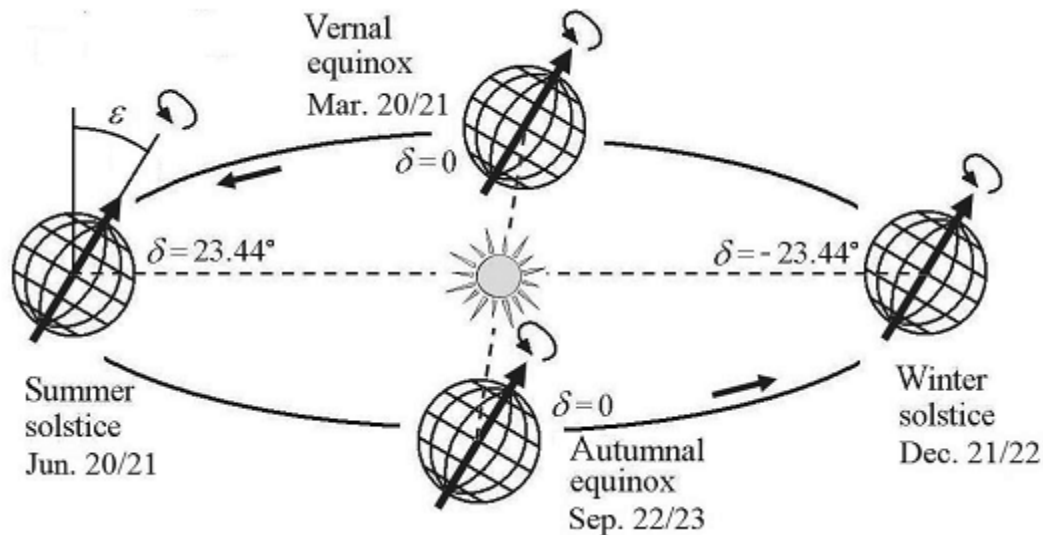


Figure II.6: Earth's orbit and the declination angle δ .

The angle between the Sun direction and the equatorial plane is called the declination angle δ and varies throughout the year from $+23.44^\circ$ when the summer solstice (June 20/21) to -23.44° at the winter solstice (December 21/22). On March 21st, and respectively, September 22/23 the declination $\delta = 0$.

II.2.4 Ground measurements of solar radiation

Radiometry is the science of electromagnetic radiation measurement. The generic device is named radiometer. For instance, the pyrheliometer that measures the direct beam irradiance and the pyranometer that measures the horizontal beam and diffuse irradiances.

II.2.4.1 Pyrheliometer

The pyrheliometer is a broadband instrument that measures the direct beam component G_n of solar radiation. Consequently, the instrument should be permanently pointed toward the Sun. A two-axis Sun tracking mechanism is most often used for this purpose. The detector is a multi-junction thermopile placed at the bottom of a collimating tube (Figure II.7a) provided with a

quartz window to protect the instrument. The detector is coated with optical black paint (acting as a full absorber for solar energy in the wavelengths range 0.280–3 μm). Its temperature is compensated to minimize sensitivity of ambient temperature fluctuations. The pyrheliometer aperture angle is 5°. Consequently, radiation is received from the sun and a limited circumsolar region, but all diffuse radiation from the rest of the sky is excluded. A readout device is used to give the instant value of the direct beam irradiance. Its scale is adapted to the sensitivity of the particular instrument in order to display the value in SI units, Wm^{-2} . For illustration, a picture of a Hukseflux DR01 First Class pyrheliometer (Hukseflux 2012) is presented in Figure II.7b.

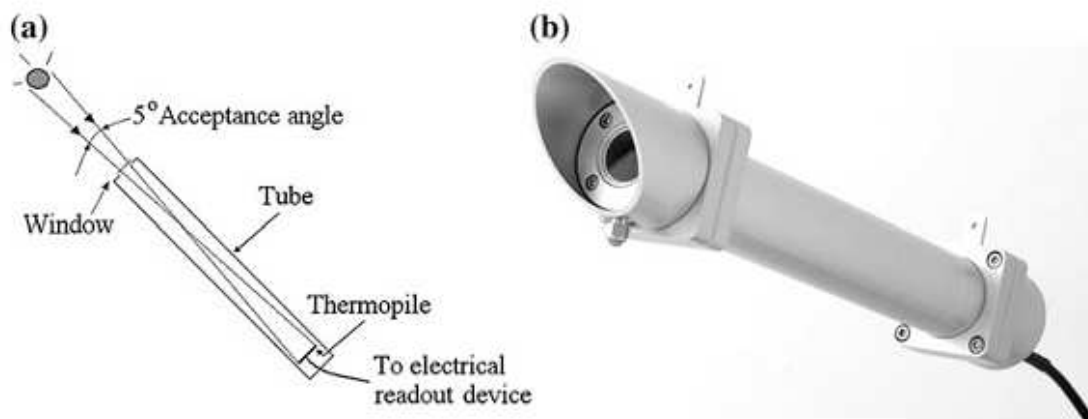


Figure II.7:a Schematic of a pyrheliometer. b Photo of Hukseflux DR01 first class pyrheliometer (Hukseflux 2012). (Public license on Wikimedia commons).

II.2.4.2 Pyranometer

Pyranometers are broadband instruments that measure global solar irradiance incoming from a 2π solid angle on a planar surface. A typical pyranometer is schematically represented in Figure II.8a. It consists of a white disk for limiting the acceptance angle to 180° and two concentric hemispherical transparent covers made of glass. The two domes shield the sensor from thermal convection, protect it against weather threat (rain, wind, and dust) and limit the spectral sensitivity of the instrument in the wavelength range [0.29–2.8 μm]. A cartridge of silica gel inside the dome absorbs water vapor.

A pyranometer can be also used to measure the diffuse solar irradiance G_d , provided that the contribution of the direct beam component is eliminated. For this, a small shading disk can be mounted on an automated solar tracker to ensure that the pyranometer is continuously shaded. Alternatively, a shadow ring may prevent the direct component G_b from reaching the sensor whole day long (see Figure II.8b). Because the daily maximum Sun elevation angle changes day by day, it is necessary to change periodically (days lag) the height of the shadow ring.

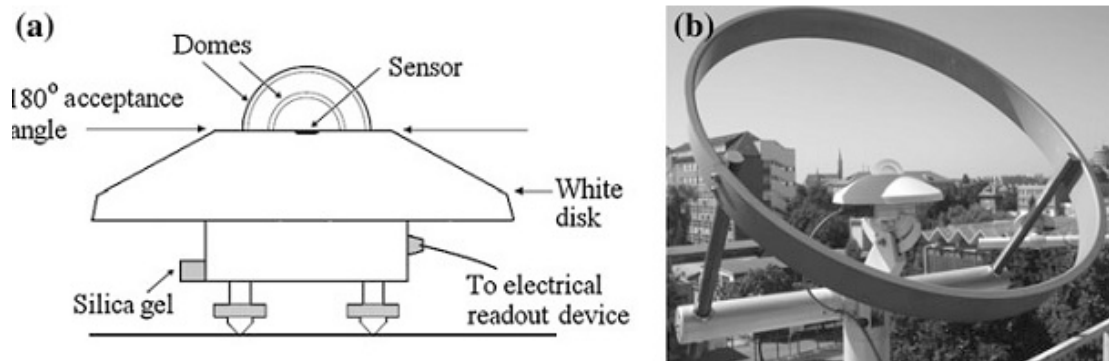


Figure II.8:(a) Schematic of a pyranometer. (b) First class pyranometer LPPYRA 12 (DeltaOHM 2012) equipped with shadow ring, mounted on the solar platform of the West University of Timisoara, Romania (SRMS 2012).

II.3 p-n Junctions

P-n junctions consist of two semiconductor regions of opposite type. Such junctions show a pronounced rectifying behavior. They are also called p-n diodes in analogy with vacuum tubes.

The p-n junction is a versatile element, which can be used as a rectifier, as an isolation structure and as a voltage-dependent capacitor. In addition, they can be used as solar cells, photodiodes, light emitting diodes and even laser diodes.

II.3.1 Structure and principle of operation

A p-n junction consists of two semiconductor regions with opposite doping type as shown in Figure II.9. The region on the left is *p*-type with an acceptor density N_a , while the region on the right is *n*-type with a donor density N_d . The dopants are assumed to be shallow, so that the electron (hole) density in the *n*-type (*p*-type) region is approximately equal to the donor (acceptor) density.

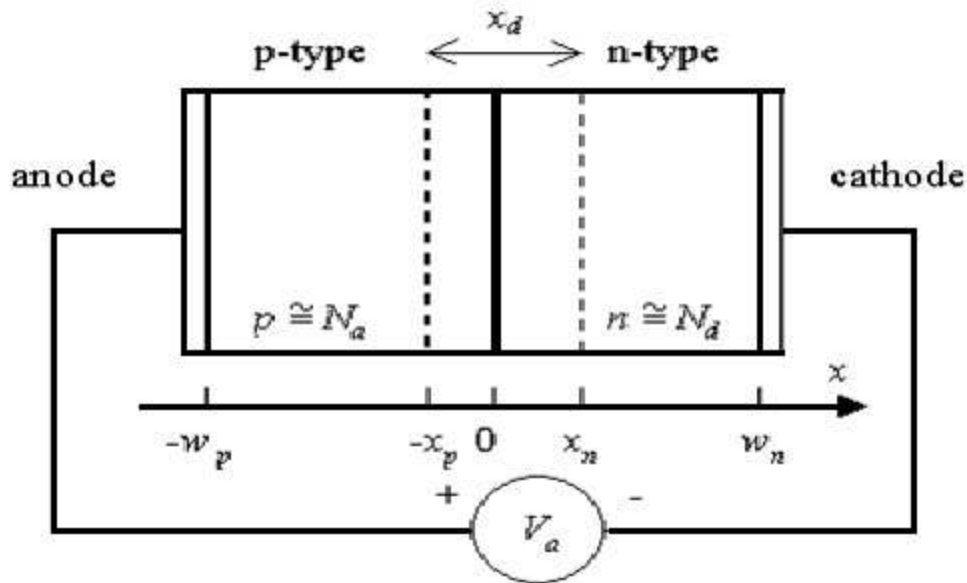


Figure II.9: Cross-section of a p-n junction.

We will assume, unless stated otherwise, that the doped regions are uniformly doped and that the transition between the two regions is abrupt. We will refer to this structure as an abrupt p-n junction.

Frequently we will deal with p-n junctions in which one side is distinctly higher-doped than the other. We will find that in such a case only the low-doped region needs to be considered, since it primarily determines the device characteristics. We will refer to such a structure as a one-sided abrupt p-n junction.

The junction is biased with a voltage V_a as shown in Figure II.9. We will call the junction forward-biased if a positive voltage is applied to the p-doped region and reversed-biased if a negative voltage is applied to the p-doped region. The contact to the p-type region is also called the anode, while the contact to the n-type region is called the cathode, in reference to the anions or positive carriers and cations or negative carriers.

II.3.2 Flatband diagram

The principle of operation will be explained using a thought experiment, an experiment, which is in principle possible but not necessarily executable in practice. We imagine that one can bring both semiconductor regions together, aligning both the conduction and valence band energies of each region. This yields the so-called flatband diagram shown in Figure II.10.

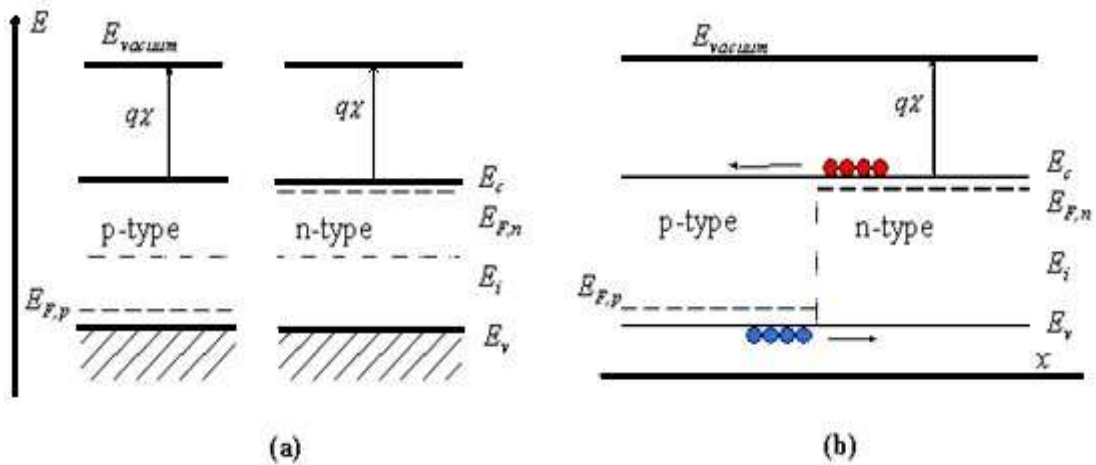


Figure II.10: Energy band diagram of a p-n junction (a) before and (b) after merging the n-type and p-type regions.

Note that this does not automatically align the Fermi energies, $E_{F,n}$ and $E_{F,p}$. Also, note that this flatband diagram is not an equilibrium diagram since both electrons and holes can lower their energy by crossing the junction. A motion of electrons and holes is therefore expected before thermal equilibrium is obtained. The diagram shown in Figure II.10 (b) is called a flatband diagram. This name refers to the horizontal band edges. It also implies that there is no field and no net charge in the semiconductor.

II.3.3 Thermal equilibrium

To reach thermal equilibrium, electrons/holes close to the metallurgical junction diffuse across the junction into the p-type/n-type region where hardly any electrons/holes are present. This process leaves the ionized donors (acceptors) behind, creating a region around the junction, which is depleted of mobile carriers. We call this region the depletion region, extending from $x = -x_p$ to $x = x_n$. The charge due to the ionized donors and acceptors causes an electric field, which in turn causes a drift of carriers in the opposite direction. The diffusion of carriers continues until the drift current balances the diffusion current, thereby reaching thermal equilibrium as indicated by a constant Fermi energy. This situation is shown in Figure II.11:

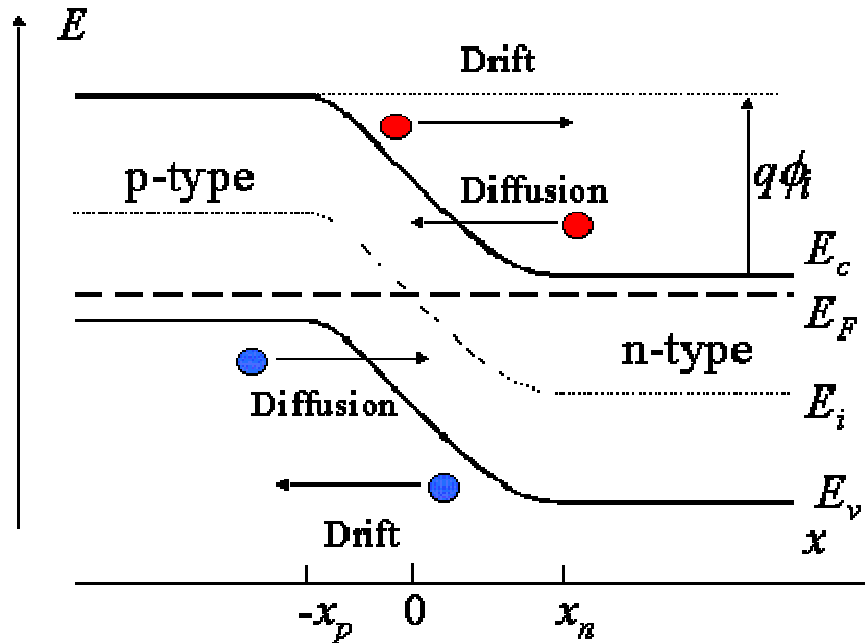


Figure II.11: Band Diagram of p-n Junction in Thermal Equilibrium [38].

II.3.4 Forward and reverse bias

We now consider a p-n diode with an applied bias voltage, V_a . A forward bias corresponds to applying a positive voltage to the anode (the p-type region) relative to the cathode (the n-type region). A reverse bias corresponds to a negative voltage applied to the cathode. Both bias modes are illustrated with Figure II.12. The applied voltage is proportional to the difference between the Fermi energy in the n-type and p-type quasi-neutral regions.

As a negative voltage is applied, the potential across the semiconductor increases and so does the depletion layer width. As a positive voltage is applied, the potential across the semiconductor decreases and with it the depletion layer width. The total potential across the semiconductor equals the built-in potential minus the applied voltage, or

$$\phi = \phi_i - V_a \quad (\text{II.3})$$

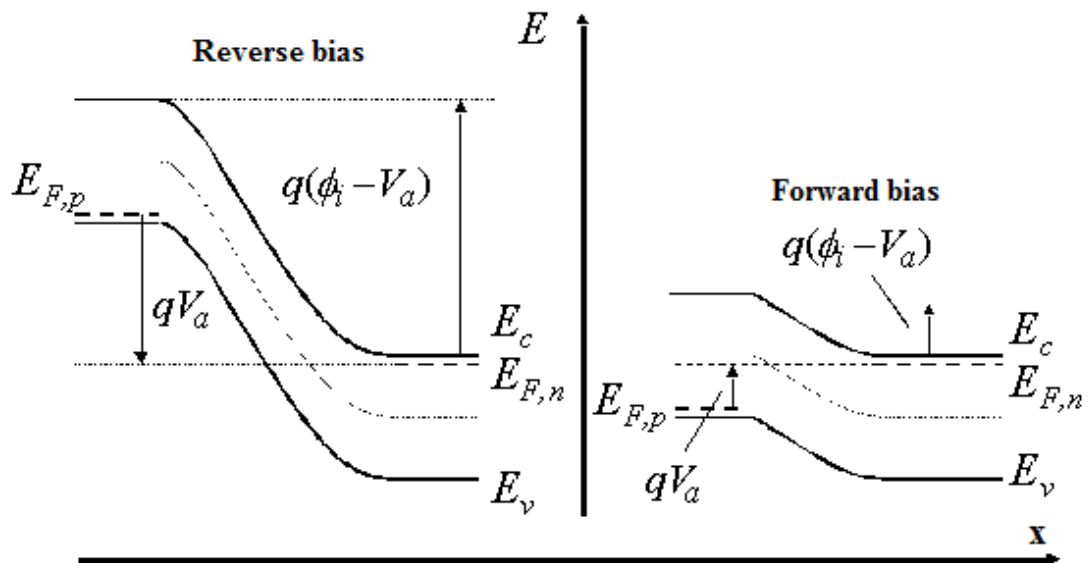


Figure II.12: Energy band diagram of a p-n junction under reverse and forward bias.

II.4 Physical processes in p-n junction of solar cells

During the illumination of the cell (junction) a number of physical processes schematically illustrated in Figure II.13 will occur:

- 1) Absorption of photons with energy $h\nu \geq E_g$
- 2) Generation of charge carrier pairs-electron and hole
- 3) Migration of charge carriers (diffusion).
- 4) Separation of charge carriers induced by built-in electric field.

The charge separation results in emerging an electric voltage on the electrodes of the solar cell.

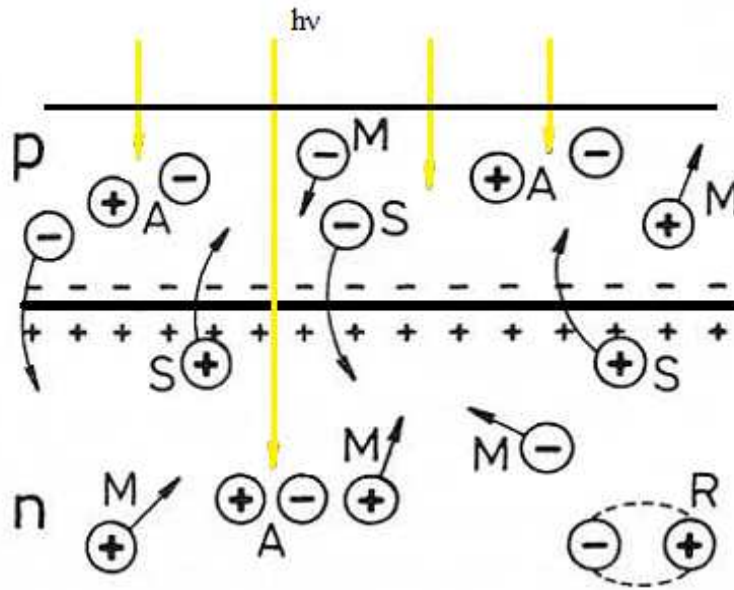


Figure II.13:Electron processes in the region of p-n junction. A- absorption of photons, M – migration of charge carriers, S – separation of electron and holes, R – recombination.

After the generation of the charge carriers (before the separation phase) the reverse and a non advantageous process – a recombination of electrons and holes could appear. Usually it is performed via defect centers. The recombination can happen in a volume of semiconductors constituting the PV structure as well as in the range of the surface. The surface recombination can be intensive and measures of reduction of these phenomena must be undertaken.

A separation effect is the final one and is the most influencing the efficiency of the PV structure and the solar cell. The effect will be the most efficient if absorption, generation of charge carriers (or quantum yield) and migration of carriers to the interface range are high and advantageous. A high level of scientific knowledge and availability of advanced technologies are needed in order to fulfill this requirement.

Absorber illuminated by the solar light absorbs photon when their energy is higher than the energy gap of the absorber. Passing distance x in a semiconductor the photon flux is absorbed according to the dependence

$$N_{ph}(x) = N_{ph}(0) (1 - r) \exp[-\alpha(\lambda)x] \quad (II.4)$$

Where r and α are coefficients of reflection and absorption, respectively.

Figure II.14 shows a plot of α vs $(h\nu)$ for several semiconductors used in fabricating solar cells.

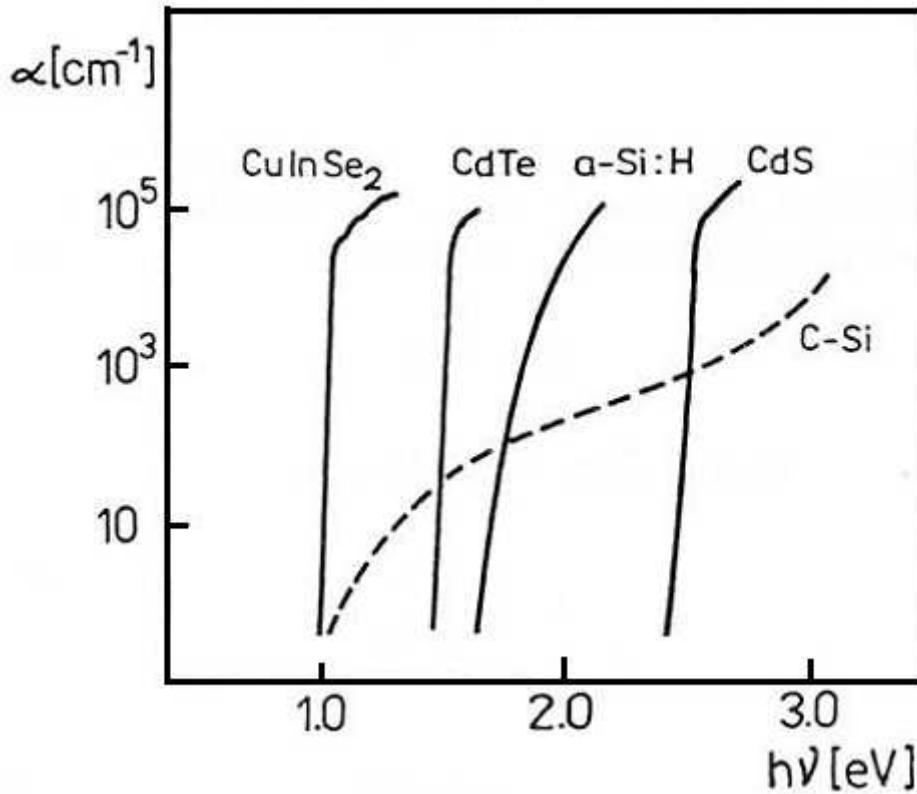


Figure II.14: Absorption edges of the photovoltaic semiconductor.

II.4.1 Equivalent circuit of the solar cell

Figure II.13 represents the equivalent circuit of a solar cell. The current through a p-n junction diode in dark is given by

$$I = I_{\text{sat}} \left(e^{\frac{qV}{nKT}} - 1 \right) \quad (\text{II.5})$$

Where I_{sat} is reverse saturation current, n is diode quality factor, V is applied voltage, K is Boltzmann constant and T is absolute temperature.

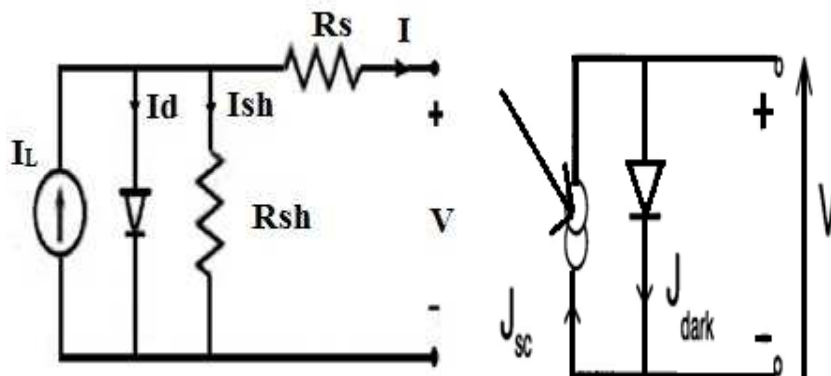


Figure II.15: Equivalent circuit of ideal solar cell and practical solar cell.

The total current flowing through the circuit is given by

$$I = -I_{gen} + I_{sat} \left[\left(\exp \left(\frac{q(V - IR_s)}{nKT} \right) \right) \right] + \frac{V - IR_s}{R_{sh}} \quad (II.6)$$

Where R_s series resistance, R_{sh} shunt resistance and I_{gen} is light generated current.

II.4.2 Solar cell parameters

The current-voltage characteristics ($I - V$) for a solar cell under dark and light condition are shown in figure II.16. The ($I - V$) curve is obtained by plotting the output current as a function of the voltage.

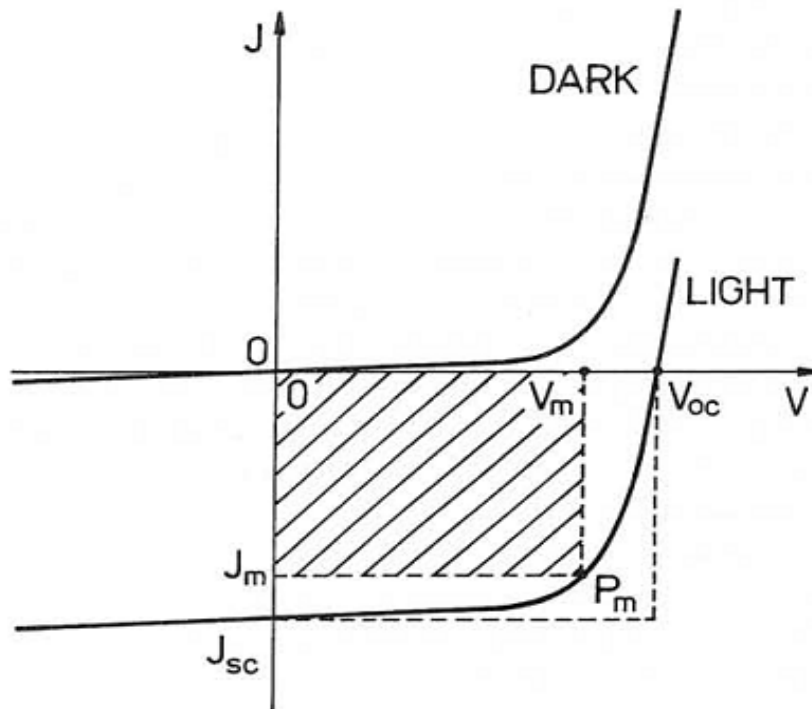


Figure II.16: The Current-voltage curve of a p-n junction solar cell.

The IV curve of a solar cell is the superposition of the IV curve of the solar cell diode in the dark with the light-generated current[39]. The light has the effect of shifting the IV curve down into the fourth quadrant where power can be extracted from the diode. Illuminating a cell adds to the normal "dark" currents in the diode so that the diode law becomes:

$$I = I_s \left[\exp \left(\frac{qV}{nKT} \right) - 1 \right] - I_{ph} \quad (II. 7)$$

Where I_{ph} light generated current and I_s Saturation current, n ideality factor.

II.4.2.1 Short circuit current (I_{sc})

The Short circuit current is found by setting $V=0$ in diode equation. This results in the following expression for I_{sc}

$$I_{sc} = - I_{gen} \quad (\text{II. 8})$$

Where I_{gen} is light generated current.

The short circuit current is normally as a current density, I_{sc} (mA/cm^2) which is given by

$$J_{sc} = \frac{I_{sc}}{A} \quad (\text{II. 9})$$

were, A is the area of the solar cell.

II.4.2.2 Open circuit voltage (V_{oc})

The open circuit voltage is given by

$$V_{oc} = A \frac{KT}{q} \ln \left(\frac{I_{gen}}{I_{sat}} + 1 \right) \quad (\text{II.10})$$

II.4.2.3 Fill factor (FF)

Another characteristic property of solar cells of interest is the fill factor, FF which is defined as

$$FF = \frac{P_m}{I_{sc} V_{oc}} = \frac{I_m V_m}{I_{sc} V_{oc}} \quad (\text{II.11})$$

Were I_m , V_m are the current and voltage at maximum power, P_m

II.4.2.4 Efficiency (η)

The efficiency of a solar cell is deefined as the ratio of light generated power from the cell to the incident power. It is a measure of light energy successfully converted to an electrical energy.

Efficiency η (%) is given by the relation.

$$\eta = \frac{P_{out}}{P_{in}} \quad (\text{II.12})$$

$$\eta = \frac{FF V_{oc} J_{sc}}{P_{in}} \quad (\text{II.13})$$

$$\eta = FF V_{oc} J_{sc} \quad (\text{II.14})$$

At 25°C , the standar reference spectrum irradiance is $100 \text{ mW}/\text{cm}^2$. So, P_{in} (Photon energy input).

II.4.2.5 Series resistance (R_s)

The current generated by photons is represented by an independent source. The two resistors are shown to model two losses in a solar cell. R_s loss is primarily due to the contact resistance of the front and back contacts of the solar cell. Other component that contributes to series resistance is resistance in the semiconductor material. Typical values of R_s are [1–5] $\Omega \text{ cm}^2$. High R_s values lead to a decrease in the solar cell which current in turn affects the efficiency.

II.4.2.6 Shunt resistance (R_{sh})

The Shunt resistance is used to model leakage currents. The shunt resistance mainly arises due leakage current created within a solar cell. Some of the reasons for the occurrence of these leakage paths are due to recombination current and surface defects in the semiconductor. These leakage paths are not uniformly distributed and vary from one cell to another. The combined effect of all the leakage paths the term called shunt resistance R_{sh} .

II.4.2.7 Quantum efficiency ($QE(\lambda)$)

For ideal solar cell, every incident photon would generate an electron-hole pair and each of the photo carriers would make it to the depletion region where they could be separated and collected. Photons with energy less than the bandgap have insufficient energy to generate photo-carriers. Even if it has the sufficient energy, it need not contribute to the photocurrent. Quantum efficiency is defined as the ratio of the number of electrons in the external circuit produced by an incident photon of given wavelength. It is the measure of the effectiveness of a device to produce electronic charge from incident photons. Quantum efficiency describes response of the device to different wavelengths of light.

$$QE(\lambda) = \frac{1}{q} \frac{hc}{\lambda} \frac{I_{sc}(\lambda)}{P(\lambda)} \quad (\text{II.15})$$

Where q is the unit charge, λ is the photon wavelength, h is Planck's constant, c is the speed of light in air, $I_{sc}(\lambda)$ is short circuit current and P is incident light power.

II.4.3 Multijunction solar cell

Multijunction cells use a combination of semiconductor materials to more efficiently capture a larger range of photon energies. They do so without sacrificing photovoltage or creating losses of heat to the degree of single-junction cells.

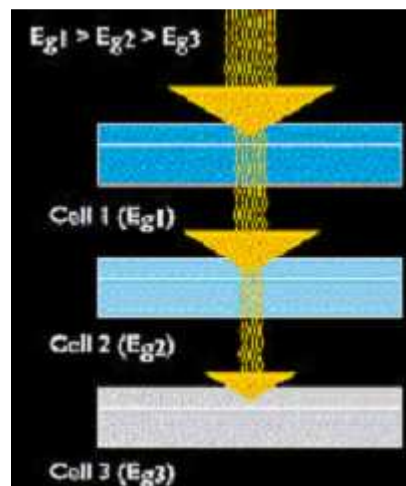


Figure II.17:A multijunction cell functions by absorbing sequentially lower energy light from the incident light.

II.4.3.1 Bandgap Selection

Consider the spectrum of sunlight split and distributed over a variety of semiconductor materials by using a prism (see Figure II.18).

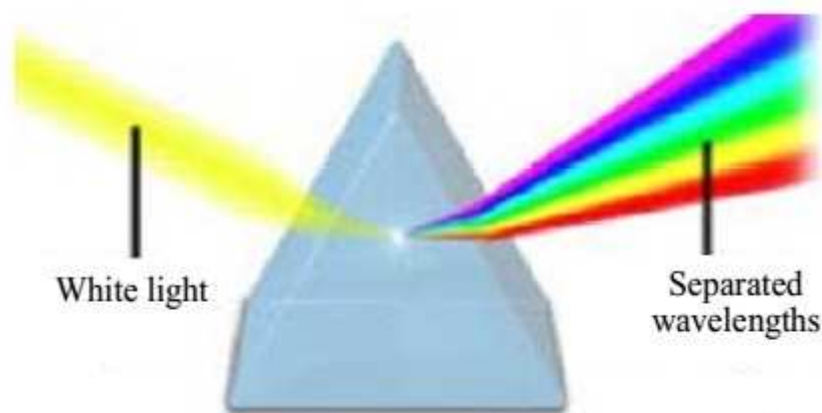


Figure II.18:Refraction of light through a prism.

In that case, a different semiconductor material could be selected (see Figure II.19a) that would best match each portion of the spectrum. Although such an arrangement is reasonable in theory, mechanically maintaining such a design would be problematic.

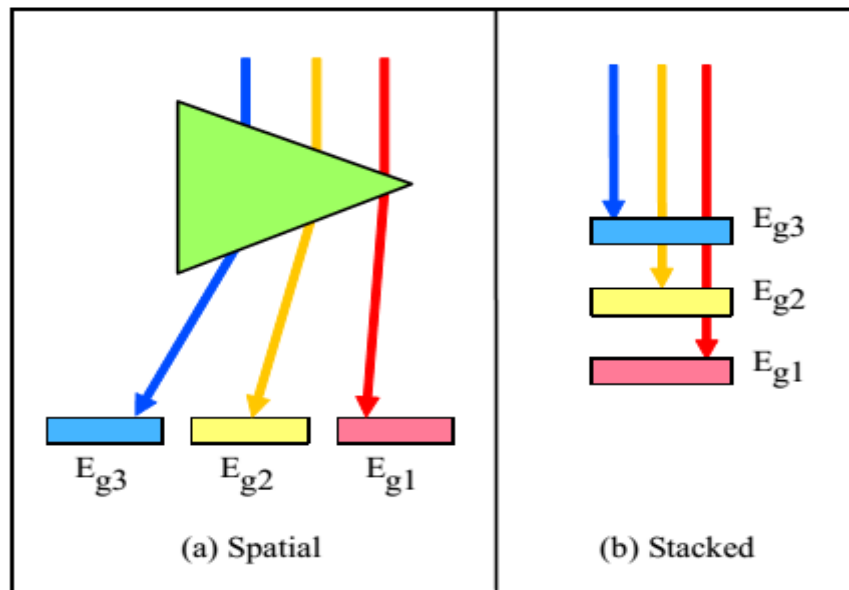


Figure II.19: Alternate configurations for multijunction spectral splitting.

A more viable solution is to stack, or grow, multiple layers of semiconductors with decreasing bandgaps (see Figure II.19b). Top layers are designed to absorb higher-energy photons while transmitting lower-energy photons that are absorbed by lower layers of the cell. In theory, a number of these layers can be so arranged. This strategy is the characteristic feature of multijunction solar cells.

Alloys of Group III and Group V elements, as well as other related compounds, lend themselves well to the design of multijunction cells. Indium Nitride (InN), Gallium Nitride (GaN), and the more commonly used GaAs are examples of such III-V materials. By carefully adjusting the compositions, a range of bandgap energies can be achieved. If a lower bandgap material were desired, less indium and more gallium would be used in the compound, up to the point at which no indium is included, and the resulting GaN would have a bandgap of about 3.4 eV.

II.5 Semiconductors

Understanding the fundamental theory behind the design of solar cells is very important for fabricating high efficiency solar cells. The main part of a solar cell is the p-n junction and the composition of the solar cell. These terms are explained in the following sections.

II.5.1 Band Theory of Solids

Atoms in a solid are closely spaced, and their outer orbitals influence one another. The result is that instead of required discrete energy levels, the outer energy levels become (smeared), forming bands of allowable energy levels. At this point, the limitations of the Bohr model of the atom as a useful model are exceeded. At this point, electrons in these bands are not associated with any particular atom. To understand the electrical properties of a material, it is helpful to consider the two bands commonly referred to as the valence band and conduction band. The valence band encompasses the energy levels at which most of the electrons (and at absolute zero, all of the electrons) will be found. Electrons found in the higher-energy conduction band are considered free electrons. Free electrons are shared among all the atoms of the solid and are not associated with any one atom. Therefore, they are very mobile. Any applied electric field can create an electrical current with these electrons.

For insulator and semiconductor materials, the valence and conduction bands are separated by a region called the bandgap. The bandgap is a region of forbidden energy levels, as defined by the quantum aspects of modern atomic theory. The difference between the lowest energy level of the conduction band and the highest energy level of the valence band is called the bandgap energy (E_g).

At temperatures above absolute zero, electrons may possess enough thermal energy (at least E_g) to be excited across the forbidden energy gap into the conduction band. This occurrence is less likely if the bandgap energy is large, as in insulators. In conductors, the conduction band and the valence bands overlap, and conduction of electrons occurs, even at absolute zero.

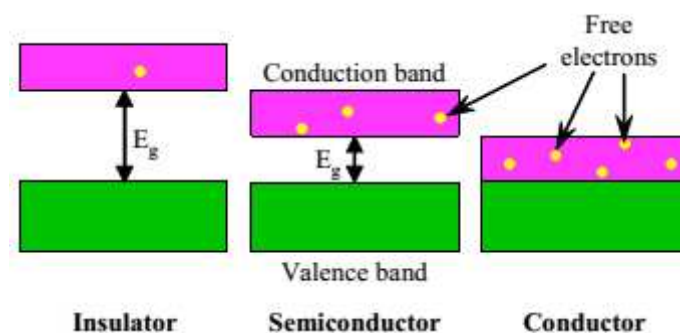


Figure II.20: Energy bandgaps.

II.5.2 Recombination and generation

When a semiconductor is disturbed from the equilibrium state the electron and hole concentrations change from their equilibrium values. A number of processes start within the

semiconductor after the perturbation in order to restore the equilibrium conditions. We call these processes recombination-generation (R-G) processes and they take care that a carrier excess or deficit is eliminated (if the perturbation is removed) or stabilized (if the perturbation is maintained). Generation is a process whereby electrons and holes are created. Recombination is a process whereby electrons and holes are annihilated or destroyed.

II.5.2.1 Band-to-band generation

The generation of an electron-hole pair can occur when the energy to break a bond is delivered by a photon (photogeneration) or by heat (direct thermal generation). This process can be visualized in terms of the band diagram as the excitation of an electron from the valence band into the conduction band.

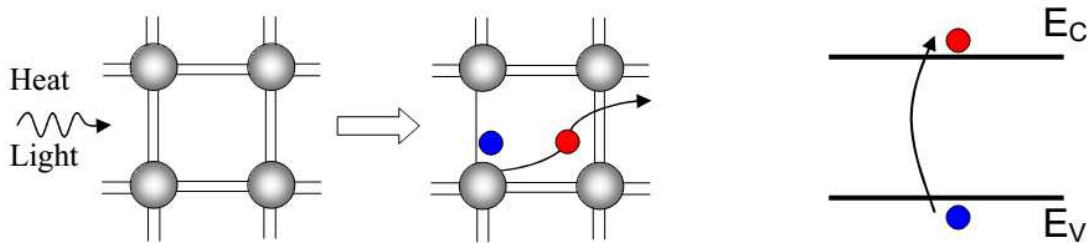


Figure II.21: photogeneration and direct thermal generation.

II.5.2.2 Band-to-band recombination

This process involves the direct annihilation of a conduction-band electron with a valence-band hole and is often called direct thermal recombination. It is typically a radiative process, in which a photon is emitted that carries an excess energy released in the recombination process.

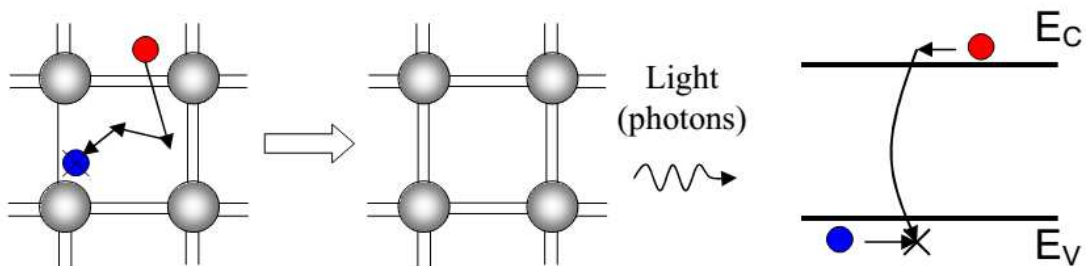


Figure II.22: direct thermal recombination.

II.5.2.3 R-G center recombination or indirect thermal recombination

As the name suggests the annihilation or creation of electrons and holes does not occur directly but it is facilitated by a R-G center. The R-G centers can be special impurity atoms or

lattice defects. Their concentration is usually small compared to the acceptor or donor concentrations. The R-G centers introduce allowed energy levels (E_T) near the centre of the forbidden gap. An electron is trapped at the R-G center and consequently annihilated by a hole that is attracted by the trapped electron. Though this process seems to be less likely than the direct thermal recombination, it is at most operational conditions the dominant recombination-generation process in semiconductor. The process is typically non-radiative and the excess energy is dissipated into the lattice in form of heat.

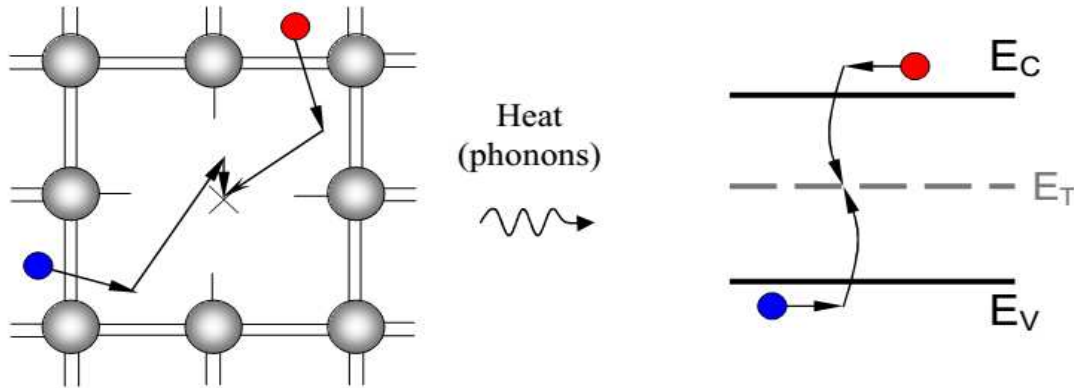


Figure II.23: R-G center (indirect thermal) recombination.

II.5.3 Equilibrium carrier concentrations

When the semiconductor is in thermal equilibrium (i.e. at a uniform temperature with no external injection or generation of carriers), the Fermi function determines the ratio of filled states to available states at each energy and is given by

$$f(E) = \frac{1}{1 + e^{(E - E_F)/kT}} \quad (\text{II.16})$$

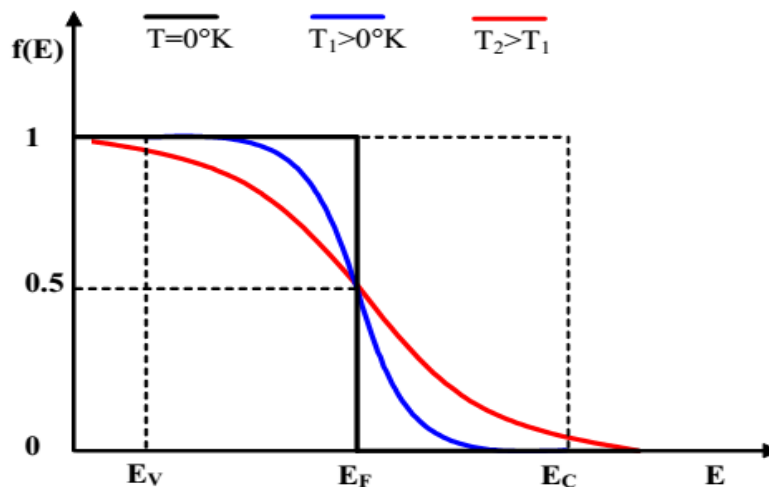


Figure II.24: The Fermi function at various temperatures.

Where E_F is the Fermi energy, k is Boltzmann's constant, and T is the Kelvin temperature. As seen in Figure II.21, the Fermi function is a strong function of temperature. At absolute zero, it is a step function and all the states below E_F are filled with electrons and all those above E_F are completely empty. As the temperature increases, thermal excitation will leave some states below E_F empty, and the corresponding number of states above E_F will be filled with the excited electrons.

The conduction-band and valence-band effective densities of state (cm^{-3}), N_C and N_V , respectively, are given by

$$N_C = 2 \left(\frac{2\pi m_n^* kT}{h^2} \right)^{3/2} \quad (\text{II.17})$$

and

$$N_V = 2 \left(\frac{2\pi m_p^* kT}{h^2} \right)^{3/2} \quad (\text{II.18})$$

When the Fermi energy, E_F , is sufficiently far ($>3kT$) from either band edge, the carrier concentrations can be well approximated (to within 2%) as [40]:

$$n_o = N_C e^{\frac{(E_F - E_C)}{KT}} \quad (\text{II.19})$$

and

$$p_o = N_V e^{\frac{(E_V - E_F)}{KT}} \quad (\text{II.20})$$

and the semiconductor is said to be nondegenerate. In nondegenerate semiconductors, the product of the equilibrium electron and hole concentrations is independent of the location of the Fermi energy and is just:

$$n_o p_o = n_i^2 = N_C N_V e^{\frac{(E_V - E_C)}{KT}} = N_C N_V e^{\frac{-E_G}{KT}} \quad (\text{II.21})$$

where n_i is the intrinsic carrier concentration.

In an undoped (intrinsic) semiconductor in thermal equilibrium, the number of electrons in the conduction band and the number of holes in the valence band are equal; $n_o = p_o = n_i$, where n_i is the intrinsic carrier concentration. The intrinsic carrier concentration can be computed from equation :

$$n_i = \sqrt{N_C N_V} e^{\frac{(E_V - E_C)}{2KT}} = \sqrt{N_C N_V} e^{\frac{-E_G}{2KT}} \quad (\text{II.22})$$

The Fermi energy in an intrinsic semiconductor, $E_i = E_F$, is given by:

$$E_i = \frac{E_V + E_C}{2} + \frac{KT}{2} \ln \left(\frac{N_V}{N_C} \right) \quad (\text{II.23})$$

Under assumption that the semiconductor is uniformly doped and in equilibrium a simple relationship between the carrier and dopant concentrations can be established. We assume that at room temperature the dopant atoms are ionized. Inside a semiconductor the local charge density is given by:

$$\rho = q (p + N_D^+ - n - N_A^-) \quad (\text{II.24})$$

where q is the elementary charge ($q = 1.602 \times 10^{-19}$ C). Under equilibrium conditions, in the uniformly doped semiconductor the local charge is zero, which means that the semiconductor is everywhere charge-neutral. One can write:

$$p + N_D^+ - n - N_A^- = 0 \quad (\text{II.25})$$

As previously discussed, the thermal energy available at room temperature is sufficient to ionise almost all the dopant atoms. Under this assumption, $N_D^+ \approx N_D$ and $N_A^- \approx N_A$, one obtains:

$$p + N_D - n - N_A = 0 \quad (\text{II.26})$$

which is the common form of the charge neutrality equation.

The position of the Fermi level in semiconductor :

$$E_C - E_F = KT \ln \left(\frac{N_C}{N_D} \right) \quad \text{for n-type} \quad (\text{II.27}) \quad E_F - E_V = KT \ln \left(\frac{N_V}{N_A} \right) \quad \text{for p-type} \quad (\text{II.28})$$

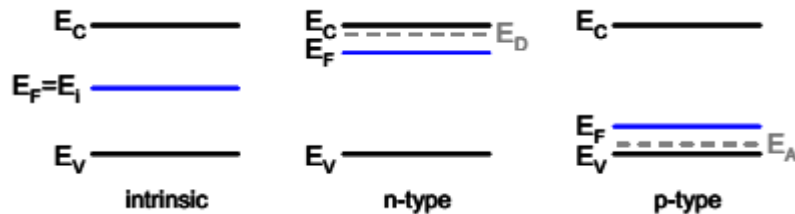


Figure II.25: A shift of the position of the Fermi energy in the band diagram and the introduction of the allowed energy level into the bandgap due to the doping.

Chapter III

The SILVACO ATLAS Simulator

III.1 Introduction

SILVACO (Silicon Valley Corporation) is an American company, headquartered in Santa Clara, California. It is a leading provider of business software string simulation and finite element aided design for electronics technology TCAD (Technology Computer Aided Design). These tools are used by companies in the microelectronics research, development and design of devices.

The edition number and the issue date is shown below

- Edition 1 - July 1, 1993.
- Edition 2 - March 1, 1994.
- Edition 3 - June 1, 1994.
- Edition 4 - October 30, 1996.
- Edition 5 - April 30, 1997.
- Edition 6 - November 1998.
- Edition 7 - February 2000.
- Edition 8 - December 2002.
- Edition 9 - September 2004.

III.2 Silvaco Atlas Simulation Software

Has ability to accurately simulate a semiconductor device is crucial for industry and research communities. The ATLAS simulation tool is specially designed for 2D and 3D modeling based on the physics of semiconductor components, including electrical, optical and thermal properties. It has a library of predefined materials as it allows the user to define their own other choice materials.

III.2.1 Atlas Inputs and Outputs

Atlas uses two types of input file:

- A text file that contains Atlas commands.
- A structure file that defines the structure to be simulated.

Atlas produces three types of output files:

Chapter III The SILVACO ATLAS Simulator

- The runtime output that gives error and warning messages as the simulation proceeds.
- The log file that stores voltages and currents.
- The structure file that stores 2D and 3D data relating to the values of solution variables

The inputs and outputs for Silvaco Atlas are depicted in Figure III.1

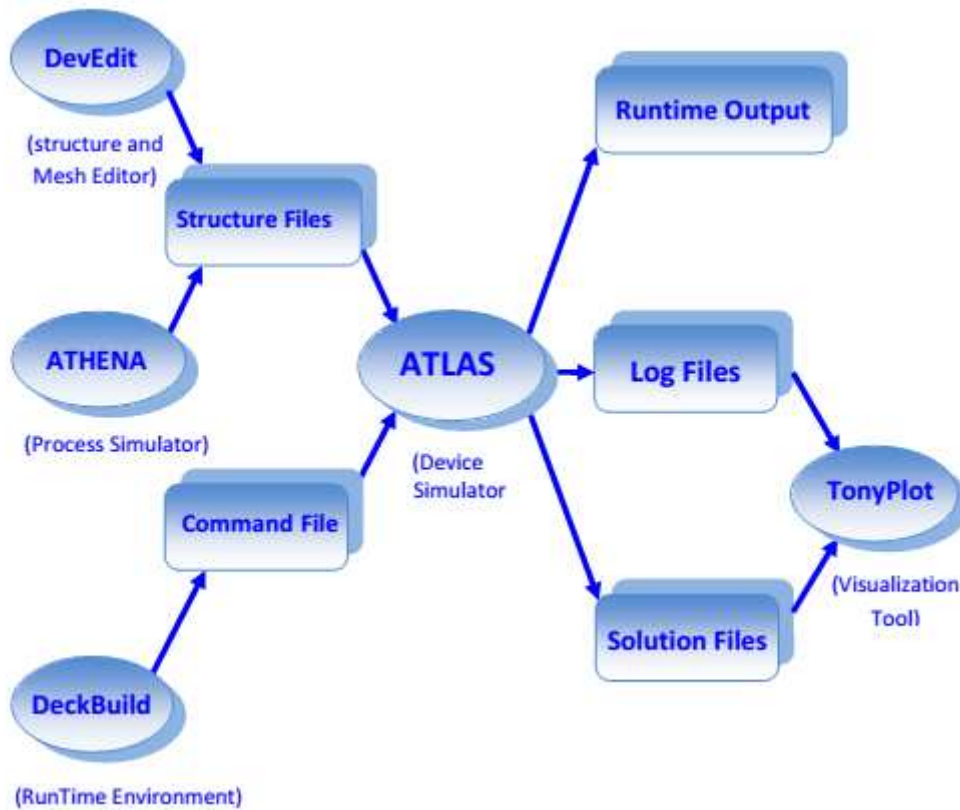


Figure III.1: Atlas inputs and outputs [41].

III.2.2 Using "Silvaco-Atlas" software

Included in the "Atlas" physical models [42]:

- DC, AC small-signal, and full time-dependency.
- Drift-diffusion transport models.
- Energy balance and Hydrodynamic transport models.
- Lattice heating and heatsinks.
- Graded and abrupt hetero-junctions.
- Optoelectronic interactions with general ray tracing.
- Amorphous and polycrystalline materials.
- General circuit environments.
- Stimulated emission and radiation

Chapter III The SILVACO ATLAS Simulator

- Fermi-Dirac and Boltzmann statistics.
- Advanced mobility models.
- Heavy doping effects.
- Full acceptor and donor trap dynamics
- Ohmic, Schottky, and insulating contacts.
- SRH, radiative, Auger, and surface recombination.
- Impact ionization (local and non-local).
- Floating gates.
- Band-to-band and Fowler-Nordheim tunneling.
- Hot carrier injection.
- Quantum transport models
- Thermionic emission currents.

III.2.3 Running Atlas inside Deckbuild

To run Atlas inside Deckbuild use the following command line:

```
> go atlas
```

III.2.4 Input file structure

Following that command, the input file needs to follow a pattern in Figure III.2

Group		commands
1. Structure specification	————	MESH REGION ELECTRODE DOPING
2. Materials model specification	————	MATERIAL MODELS CONTACT INTERFACE
3. Method selection	————	METHOD
4. Solution specification	————	LOG SOLVE LOAD SAVE
5. Results analysis	————	EXTRACT TONYPLOT

Figure III.2: Atlas command groups [43].

III.3 Structure Specification

The structure specification is done by defining the mesh, the region, the electrodes and the doping levels.

III.3.1 Mesh

The mesh used for this thesis is two-dimensional. Therefore, only x and y parameters are defined. The mesh is a series of horizontal and vertical lines and spacing between them. From Figure III.3, the mesh statements are specified.

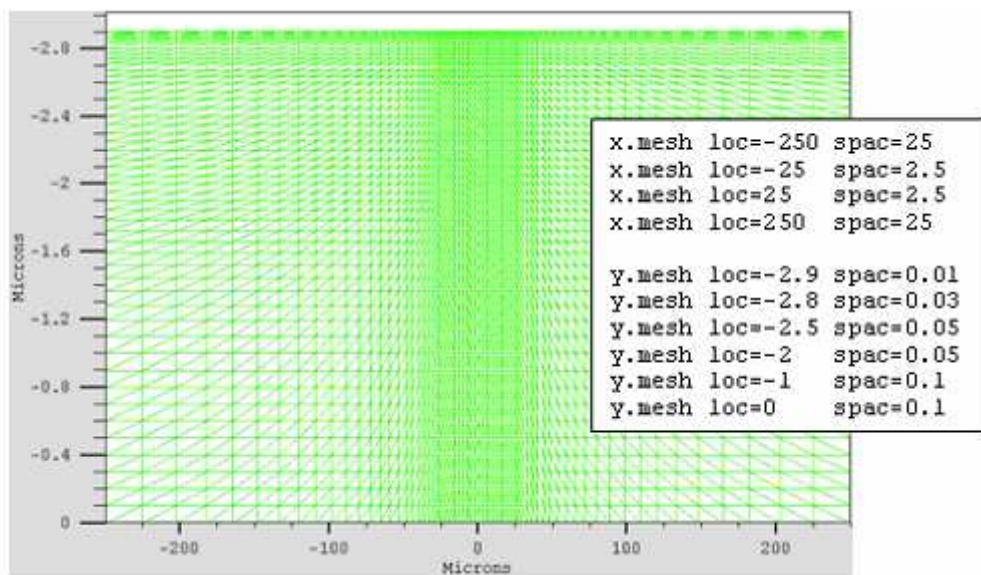


Figure III.3: Atlas mesh.

The general format to define the mesh is:

X.MESH LOCATION=<VALUE> SPACING=<VALUE>

Y.MESH LOCATION=<VALUE> SPACING=<VALUE>

For example, the x.mesh starting at -250 microns has spacing of 25 microns. That means it is relatively coarse. The x.mesh becomes finer between -25 and 25 microns with a spacing of 2.5 microns. The y.mesh is similarly defined. For example, at y.mesh of -2.9 microns, the spacing is 0.01 microns. Then at location y.mesh of -2.8 microns, the spacing changes to 0.03 microns. The mesh is coarser at y.mesh location of -1, when the spacing is 0.1.

A coarse or fine mesh determines the accuracy of the simulation. A coarse mesh produces a faster simulation, but less accurate results. A fine mesh produces a slower simulation, but more accurate results. The areas that have a finer mesh, therefore, are of greatest interest in the simulation.

III.3.2 Region

After defining the mesh, it is necessary to define the regions. The format to define the regions is as follows:

```
REGION number=<integer><material_type> /  
<position parameters>
```

From Figure III.4, the code that defines the regions is identified. There are six regions defined. The limits of each region are explicitly identified in the x- and y-axis. The regions must then be given a material.

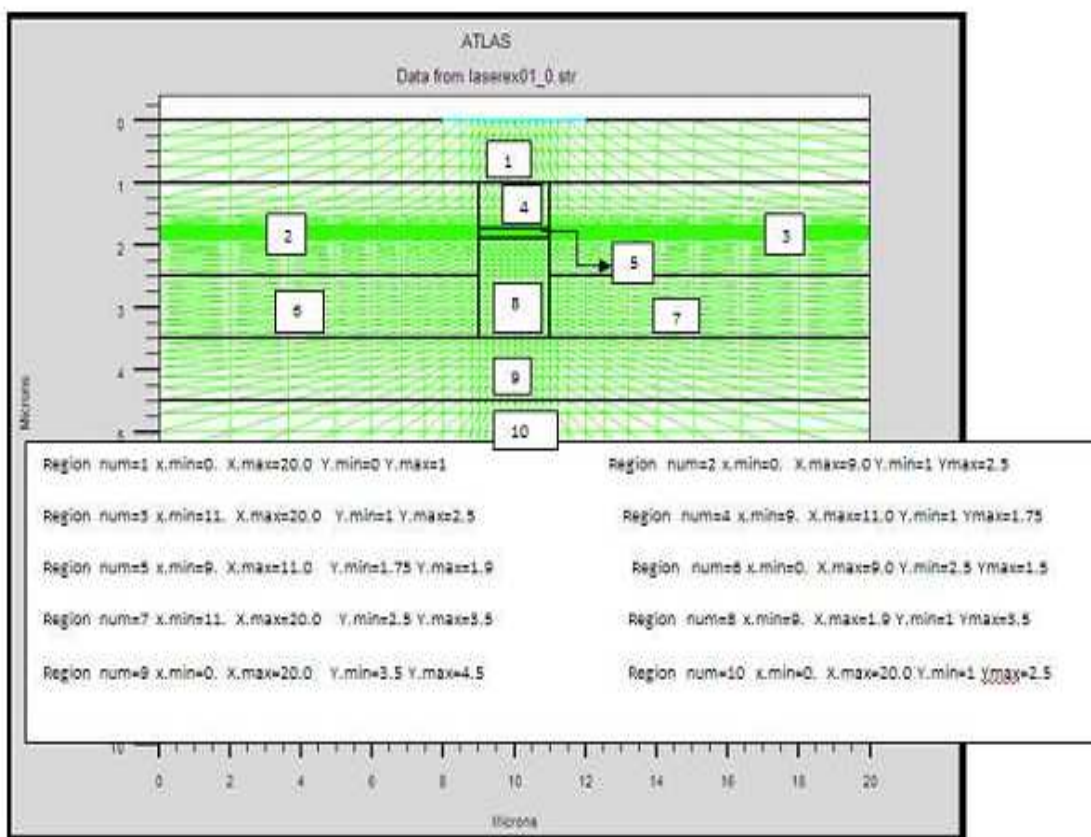


Figure III.4: Atlas region.

From Figure III.5, the code defines the material for each region. Note that the color coding identifies the material. The regions have vertical and horizontal lines to mark their boundaries.

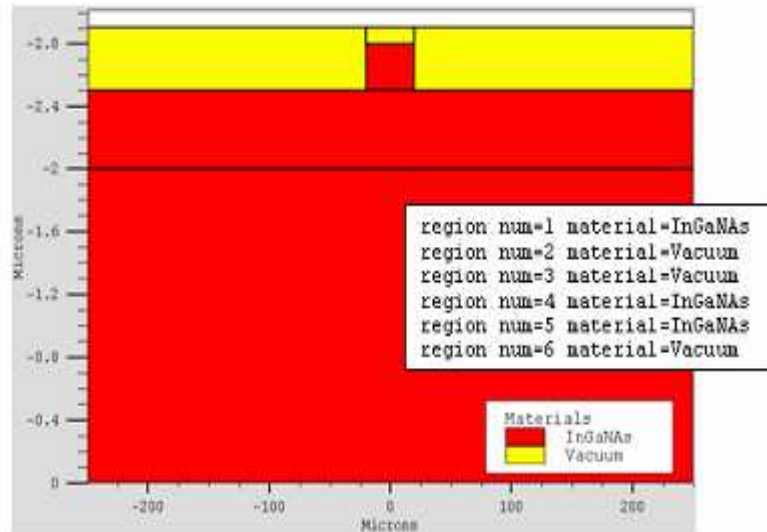


Figure III.5: Atlas regions with materials defined [44].

III.3.3 Electrodes

The next structure specification corresponds to electrodes. Typically, in this simulation the only electrodes defined are the anode and the cathode. However, Silvaco Atlas has a limit of 50 electrodes that can be defined. The format to define electrodes is as follows:

ELECTRODE NAME=<electrode name><position_parameters>

From Figure III.6, the electrode statements are defined for the anode and the cathode. Note that the cathode is defined with gold as the material. The x and y dimensions correspond to region 6 previously defined. Meanwhile, the anode is defined at the bottom of the cell for the entire xrange at y=0.

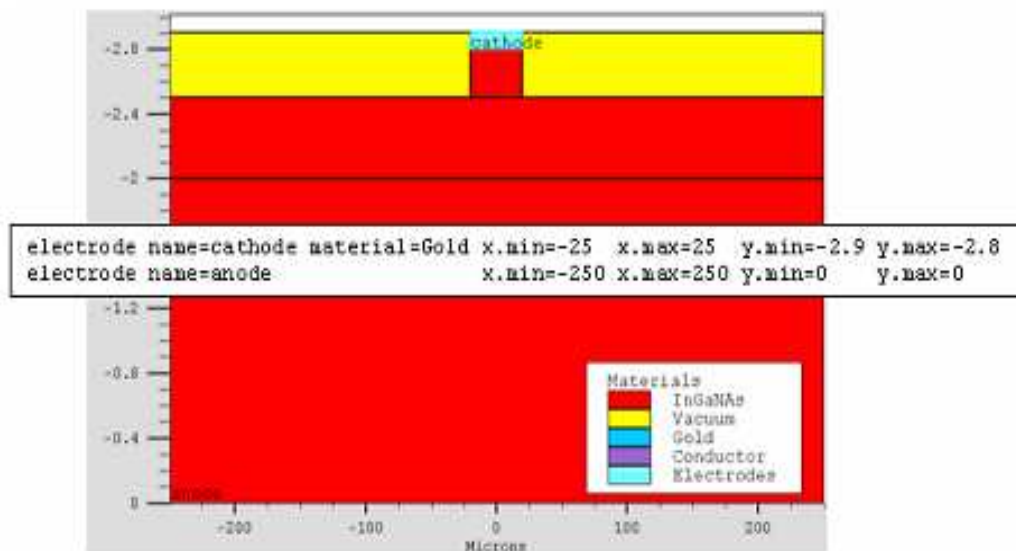


Figure III.6: Atlas electrodes [45].

III.3.4 Doping

The last aspect of structure specification that needs to be defined is doping. The format of the Atlas statement is as follows:

```
DOPING <distribution type><dopant_type> /  
<position parameters>
```

From Figure III.7, the doping types and the doping levels are defined. Doping can be n-type or p-type. The distribution type can be uniform or Gaussian.

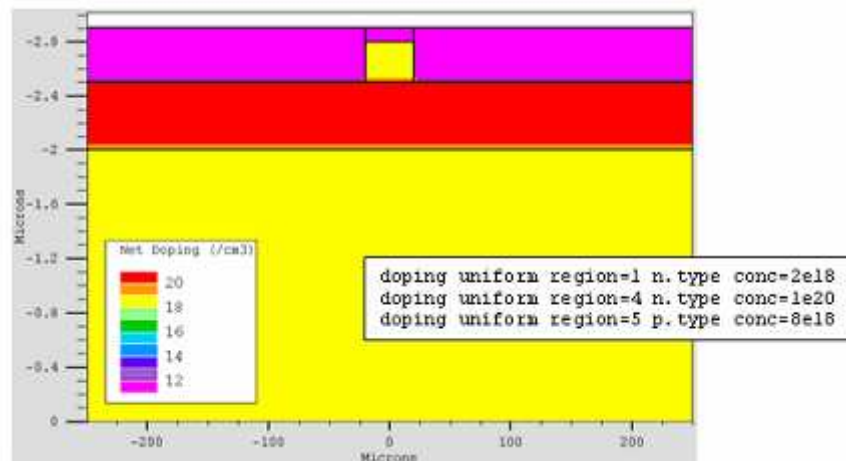


Figure III.7: Atlas electrodes [46].

III.3.5 Materials Model Specification

After the structure specification, the materials model specification is next.

III.3.5.1 Material

The format for the material statement is as follows:

```
MATERIAL <localization><material_definition>
```

Below are three examples of the material statement:

```
MATERIAL MATERIAL=Silicon EG300=1.1 MUN=1200
```

```
MATERIAL REGION=4 TAUN0=3e-7 TAUP0=2e-5
```

```
MATERIAL NAME=base NC300=4e18
```

In all examples, when MATERIAL appears first, it is considered the statement. When MATERIAL appears a second time in the first example, it is considered a localization parameter. In the second and third examples, the localization parameters are REGION and NAME, respectively. Various other parameters can be defined with the material statement. Examples of these parameters are the band gap at room temperature (EG300), electron mobility (MUN),

Chapter III The SILVACO ATLAS Simulator

electron (TAUN0) and hole (TAUP0) recombination lifetimes, conduction band density at room temperature (NC300), among others.

III.3.5.2 Models

The physical models fall into five categories: mobility, recombination, carrier statistics, impactionization, and tunneling. The syntax of the model statement is as follows:

```
MODELS <model flag><general parameter> /  
<model dependent parameters>
```

The choice of model depends on the materials chosen for simulation. The example below activates several models.

```
MODELS CONMOB FLDMOB SRH
```

Table III.1 shows some models.

Table III.1: Examples of models in Silvaco

Model	Syntax	Notes
Concentration Dependent	conmob	It is a doping versus mobility table valid for 300K only.
Concentration and Temperature Dependent	analytic	Caughey - Thomas formula. Tuned for 77-450K.
Carrier-Carrier Scattering	ccsmob	Important when carrier concentration is high (e.g., forward bias power devices).
Parallel Electric Field Dependence	fldmob	Required to model any type of velocity saturation effect.

III.3.5.3 Contact

Contact determines the attributes of the electrode. The syntax for contact is as follows:

```
CONTACT NUMBER=<n> |NAME=<ename>|ALL
```

The following is an example of the contact statement.

```
CONTACT NAME=anode current.
```

III.3.5.4 Interface

The semiconductor or insulator boundaries are determined with the interface statement. The syntax is as follows:

```
INTERFACE [<parameters>]
```

The following example shows the usage of the interface statement.

```
INTERFACE X.MIN=-4 X.MAX=4 Y.MIN=-0.5 Y.MAX=4 \  
QF=1e10 S.N=1e4 S.P=1e4
```

III.3.6 Numerical Method Selection

After the materials model specification, the numerical method selection must be specified. There are various numerical methods to calculate solutions to semiconductor device problems. There are three types of solution techniques used in Silvaco Atlas:

- decoupled (GUMMEL)
- Fully coupled (NEWTON)
- BLOCK

The Gummel method solves for each unknown in turn, keeping the other variables constant and repeating the process until a stable solution is achieved.

- This method tolerates relatively poor initial guess.
- Generally, it is useful where the system of equations is weakly coupled but has only linear convergence.
- It cannot be used with lumped elements or current boundary conditions.

The Newton method solves the total system of unknowns together. The Block method solves some equations fully coupled while others are decoupled. It is useful when lattice heating or energy balance equations are included.

The following example shows the use of the method statement.

```
METHOD GUMMEL NEWTON
```

III.3.7 Solution Specification

After completing the numerical method selection, the solution specification is next. Solution specification is broken down into log, solve, load, and save statements.

III.3.7.1 Log

Log files (.log) store the terminal characteristics calculated by Atlas. These are current and voltages at electrodes in DC simulations. In transient simulations, the time is stored. In AC simulations, the small signal frequency, the conductances and capacitances are saved.

The following shows an example of the LOG statement.

```
LOG OUTFILE=myoutputfile.log
```

The example saves the current-voltage information into myoutputfile.log.

Chapter III The SILVACO ATLAS Simulator

III.3.7.2 Solve

The SOLVE statement follows the LOG statement. SOLVE performs a solution for one or more bias points. The following is an example of the SOLVE statement.

```
SOLVE B1=10 B3=5 BEAM=1 SS.PHOT SS.LIGHT=0.01 \  
MULT.F FREQUENCY=1e3 FSTEP=10 NFSTEP=6
```

B1 and B3 specify the optical spot power associated with the optical beam numbers 1 and 3, respectively. The beam number is an integer between 1 and 10. BEAM is the beam number of the optical beam during AC photo-generation analysis. SS.PHOT is the small signal AC analysis. SS.LIGHT is the intensity of the small signal part of the optical beam during signal AC photo-generation analysis. MULT.F is the frequency to be multiplied by FSTEP. NFSTEPS is the number of times that the frequency is incremented by FSTEP.

III.3.7.3 Load and Save

The LOAD statement enters previous solutions from files as initial guess to other bias points.

The SAVE statement enters all node point information into an output file.

The following are examples of LOAD and SAVE statements.

```
SAVE OUTF=SOL.STR
```

In this case, SOL.STR has information saved after a SOLVE statement. Then, in a different simulation, SOL.STR can be loaded as follows:

```
LOAD INFILE=SOL.ST
```

III.3.8 Results Analysis

Once a solution has been found for a semiconductor device problem, the information can be displayed graphically with TonyPlot. Additionally, device parameters can be extracted with the EXTRACT statement. To generate the Extract statement:

Select Extract → Device... from the Command menu

In the example below, the EXTRACT statement obtains the current and voltage characteristics of a solar cell. This information is saved into the IVcurve.dat file. Then, TonyPlot plots the information in the IVcurve.dat file.

```
EXTRACT NAME="iv" curve(v."anode", I."cathode") /  
OUTFILE="IVcurve.dat"  
TONYPLOTIVcurve.dat
```

Chapter IV

Results and discussions

IV.1 Introduction

This work is to study the transport of electrical charges in a solar cell based on Indium Gallium Nitride (InGaN). By varying the alloy composition (Ga replaced by In), InGaN can reach all values of bandgap between 3.40 eV and 0.7eV, which covers almost the entire solar spectrum. At present most of the studies of InGaN photovoltaics are conducted on hetero structures. The aim of this study is therefore to better understand the influence of each parameter of the solar cell for an improved optimization of performance. In this chapter we will present the simulation results of the effect of the In proportion on the InGaN solar cell performance.

IV.2 Model description

In this work, calculations were all performed under 1-sun AM1.5 illumination, that is with an input power of $P_{in} = 1000 \text{ W/m}^2$ and a temperature of 300 K using one p-n-junction as shown in figure IV.1.

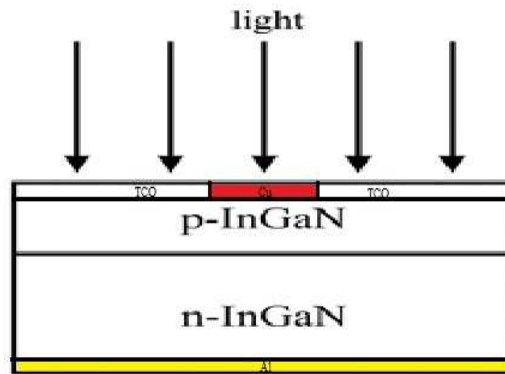


Figure IV.1: Structure of an InGaN solar cell.

IV.3 Simulation parameters

A general expression for the wavelength-dependent absorption coefficient [47] of $\text{In}_x\text{Ga}_{1-x}\text{N}$ used in the simulation is given as

$$\alpha(\text{cm}^{-1}) = 10^5 x \left[C(E_{ph} - E_g) + D(E_{ph} - E_g)^2 \right]^{1/2} \quad (\text{IV.1})$$

Where E_{ph} is the photon energy, C and D are composition dependent parameters given in table IV.1 for $\text{In}_x\text{Ga}_{1-x}\text{N}$ [48].

Chapter IV Results and discussions

Table IV.1: Fitting parameters used to calculate the absorption coefficient of $\text{In}_x\text{Ga}_{1-x}\text{N}$ alloys [49].

Indium composition	C	D
1	0.69642	0.46055
0.83	0.66796	0.68886
0.69	0.58108	0.66902
0.57	0.60946	0.62182
0.5	0.51672	0.46836
0	3.52517	0.65710

Earlier, equation (1) has been used to get best fit with experimental data of absorption coefficient of InGaN material [49]. After the compensation values C and D, E_{ph} . We find the following relationship

$$\alpha(\lambda) = 2.2 \times 10^5 \sqrt{1.24/\lambda - E_g} \quad (\text{IV.2})$$

E_g is the composition-dependent energy bandgap of $\text{In}_x\text{Ga}_{1-x}\text{N}$ (at room temperature) which is calculated as follows:

$$E_{g\text{InGaN}} = xE_{g\text{InN}} + (1-x)E_{g\text{GaN}} - bx(1-x) \quad (\text{IV.3})$$

Where x is the indium content, $E_g(\text{InN}) = 0.7$ eV, $E_g(\text{GaN}) = 3.40$ eV and the bowing parameter b is 1.43 [50].

Other modeling parameters such as permittivity (ϵ/ϵ_0), affinity (χ) and effective masses (m_e/m_h) are calculated as follows [51]:

$$\epsilon(\text{In}_x\text{Ga}_{1-x}\text{N}) = 15.3x + 8.9(1-x) \quad (\text{IV.4})$$

$$\chi(\text{In}_x\text{Ga}_{1-x}\text{N}) = 2.666x^2 + 3.659x + 4.31 \quad (\text{IV.5})$$

$$m_e(\text{In}_x\text{Ga}_{1-x}\text{N}) = 0.12x + 0.2(1-x) \quad (\text{IV.6})$$

$$m_h(\text{In}_x\text{Ga}_{1-x}\text{N}) = 0.17x + 1.0(1-x) \quad (\text{IV.7})$$

The wavelength-dependent refractive index model of Adachi given in [51] is used for $\text{In}_x\text{Ga}_{1-x}\text{N}$ as follows:

$$n(E) = \left[A \left(\frac{E_{ph}}{E_g} \right)^{-2} \left\{ 2 - \left(1 + \frac{E_{ph}}{E_g} \right)^{0.5} - \left(1 - \frac{E_{ph}}{E_g} \right)^{0.5} \right\} + B \right]^{0.5} \quad (\text{IV.8})$$

Where $A(\text{In}_x\text{Ga}_{1-x}\text{N}) = 13.55x + 9.31(1-x)$ and $B(\text{In}_x\text{Ga}_{1-x}\text{N}) = 2.05x + 3.03(1-x)$

Chapter IV Results and discussions

A general expression (as shown below) for low field mobility developed earlier by M Farahmand et al [51] is used for electron and hole mobility of III-nitride materials:

$$\mu_0(N, T) = \mu_{\min,i} \left[\frac{T}{300} \right]^{\beta_1} + \frac{(\mu_{\max,i} - \mu_{\min,i}) \left[\frac{T}{300} \right]^{\beta_2}}{1 + \left[\frac{N}{N_{\text{ref}} (T/300)^{\beta_3}} \right]^{\gamma (T/300)^{\beta_4}}} \quad (\text{IV.9})$$

Where $i = (n,p)$ or electrons and holes, respectively and N is the doping concentration, N_{ref} is fixed at $1 \times 10^{17} \text{ cm}^{-3}$, T is the temperature, β_1 , β_2 , β_3 , β_4 and γ are specific parameters for a given material [5]. For GaN, μ_{\max} and μ_{\min} values for electron (hole) mobility are 1460 (170) and $295 (5) \text{ cm}^2 \text{ V}^{-1} \cdot \text{s}^{-1}$ [51, 52] respectively. Similarly, μ_{\max} and μ_{\min} values are 3138 (340) and $774 (15) \text{ cm}^2 \text{ V}^{-1} \cdot \text{s}^{-1}$ [51], respectively, for electrons (holes) for InN material. Using these data, $\mu_0(N, T)$ is first calculated for GaN and InN material and mobility for InGaN are then linearly interpolated for electrons and holes as follows:

$$\mu_n(\text{In}_x\text{Ga}_{1-x}\text{N}) = 524x + \mu_n(\text{GaN}) \quad (\text{IV.10})$$

$$\mu_h(\text{In}_x\text{Ga}_{1-x}\text{N}) = 6.5x + \mu_h(\text{GaN}) \quad (\text{IV.11})$$

The GaN parameters, at 300 K, used in the simulation are presented in the table IV.2.

Table IV.2: The simulation parameters for GaN at 300 K

GaN used	Parameter Value
Energy bandgap (eV)	3.4
Relative permittivity ϵ	8.9
Electron mobility ($\text{cm}^2 \text{ eV}^{-1} \text{ s}^{-1}$)	1000
Hole mobility ($\text{cm}^2 \text{ eV}^{-1} \text{ s}^{-1}$)	170
Effective density of states in the conduction band $N_c (\text{cm}^{-3})$	2.3×10^{18}
Effective density of states in the valence band $N_v (\text{cm}^{-3})$	4.6×10^{19}
$N_A (\text{cm}^{-3})$	10^{18}
$N_D (\text{cm}^{-3})$	10^{17}
$W_p (\mu\text{m})$	0.01
$W_n (\mu\text{m})$	3

Table IV.3 summarises the parameters of InGaN used in the simulation

Chapter IV Results and discussions

Table IV.3: The simulation parameters for $\text{In}_x\text{Ga}_{1-x}\text{N}$ materials at 300 K.

Parameters	Expression	Reference
Energy bandgap (eV)	$0.7x + 3.7(1-x) - 1.43.x.(1-x)$	[51]
Electron mobility ($\text{cm}^2\text{eV}^{-1}\text{s}^{-1}$)	$524x + \mu_n(\text{GaN})$	[52]
Hole mobility ($\text{cm}^2\text{eV}^{-1}\text{s}^{-1}$)	$6.5x + \mu_h(\text{GaN})$	[52]
Relative permittivity ϵ	$15.3x + 8.9(1-x)$	[52]
Electron affinity $\chi(\text{eV})$	$3.659x + 2.666x^2 + 4.31$	[52]
Effective density of states in the conduction band N_c (cm^{-3})	$0.9x + 2.3(1-x)$	[52]
Effective density of states in the valence band N_v (cm^{-3})	$5.3x + 1.8(1-x)$	[52]
Absorption coefficient $\alpha(\text{cm}^{-1})$	$2.2 \times 10^5 \sqrt{1.24/\lambda - E_g}$	[52]
Carrier lifetime $\tau(\text{ns})$	1 ns	[46]
Surface recombination velocities $S_{p0}, S_{pL}, S_{n0}, S_{nL}$ (cm s^{-1})	1000	[53]

In table IV.4, we show the values of the InGaN band gap for different proportions of Indium.

Table IV.4: The InGaN band gap for different In fraction.

$x(\text{In})$	0	0.2	0.39	0.52	0.57	0.65	0.68	0.78	0.84	0.89
$E_g(\text{InGaN})$ (eV)	3.4	2.66	2.04	1.68	1.56	1.37	1.30	1.1	1	0.92

IV.4 Results and discussion

Reliable solar cell modeling should be based on accurate and reliable optical and electrical modeling parameters of the device. Hence a prerequisite to solar cell modeling is the use of a photon energy-dependent optical constant in the form of $n(E)$ (see equation (IV.8)) and $k(E)$ values where

$$k(E) = \alpha \cdot \lambda / 4\pi \quad (\text{IV.12})$$

α is absorption coefficient given in equation (IV.1) of the solar material. Such dispersion relations describing $n(E)$ and $k(E)$ of the III-N network for wide energy gaps are usually unavailable in the

Chapter IV Results and discussions

commercial SILVACO TCAD software package. We have imported these values from Adachi [54].

We have varied the In proportion to study its effect on the solar cell performance. A typical SILVACO structure output for $x=0.39$ is shown in Figure IV.2.

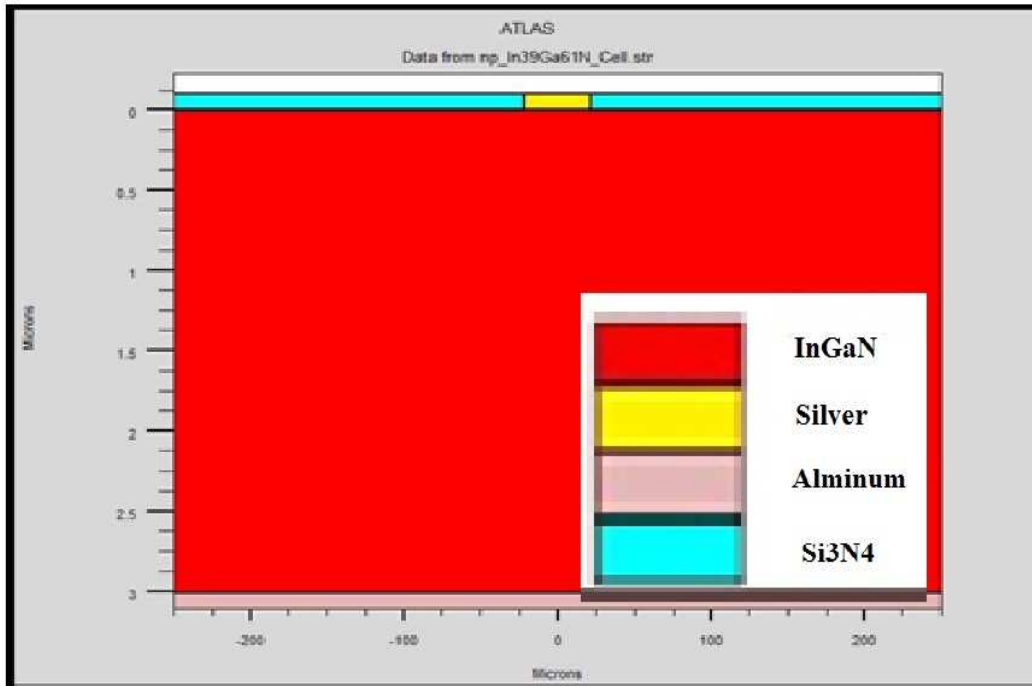


Figure IV.2: The TCO/p- InGaN/ n-InGaN sola cell with $x=0.39$.

IV.4.1 Results for proportion of indium $x=0$ (GaN)

The current density-voltage (J-V) characteristic for $x=0$ is shown in Figure IV.3.

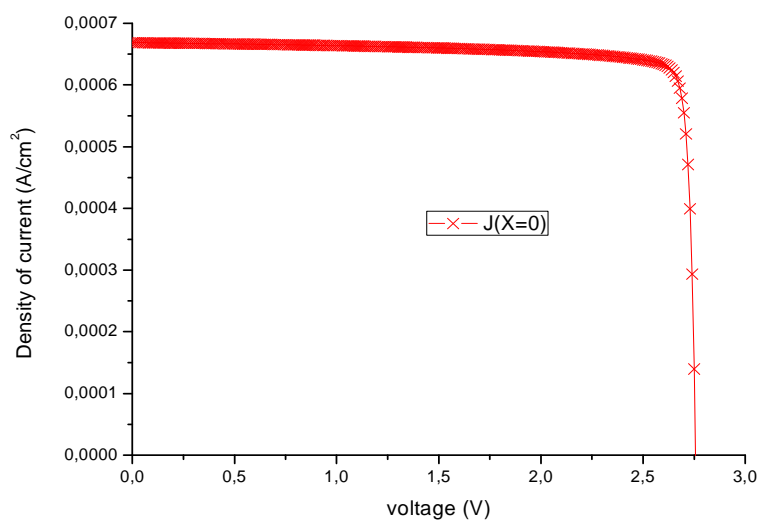


Figure IV.3: The J-V characteristic for $x=0$.

The output power-voltage characteristic for the $x=0$ is shown in Figure IV.4.

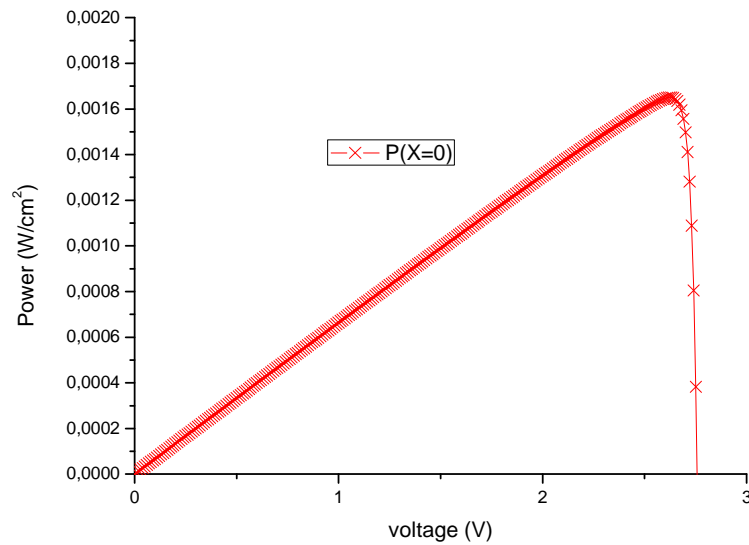


Figure IV.4: The P-V characteristic for $x=0$.

The extracted external parameters of this solar cell from the J-V and the P-V characteristics are presented in table IV.5.

Table IV.5: Parameters of p- InGaN/ n-InGaN solar cell with $x=0$.

J_{sc} (mA/cm ²)	V_{oc} (V)	J_{max} (mA/cm ²)	V_{max} (V)	P_{max} (mW/cm ²)	FF (%)	η (%)
0.67	2.76	0.63	2.63	1.65	89.3	16.50

for this percentage of indium (GaN); we have less density of current and voltage greater, this is due to the breadth in bandgap (3.4 eV), which is absorbed in the domain (UV).

IV.4.2 Results for proportion of indium $x=0.20$ ($In_{0.2}Ga_{0.8}N$)

The current density-voltage (J-V) characteristic for $x=0$ is shown in Figure IV.5.

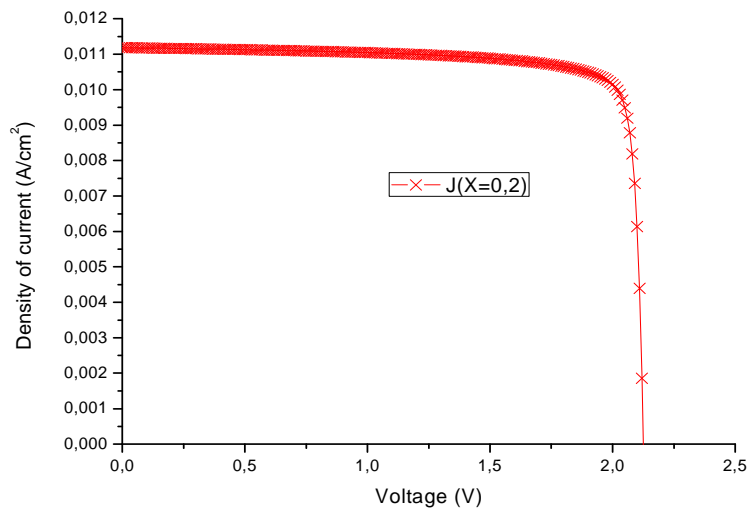


Figure IV.5: The J-V characteristic for x=0.20.

The output power-voltage characteristic for the x=0.20 is shown in Figure IV.6.

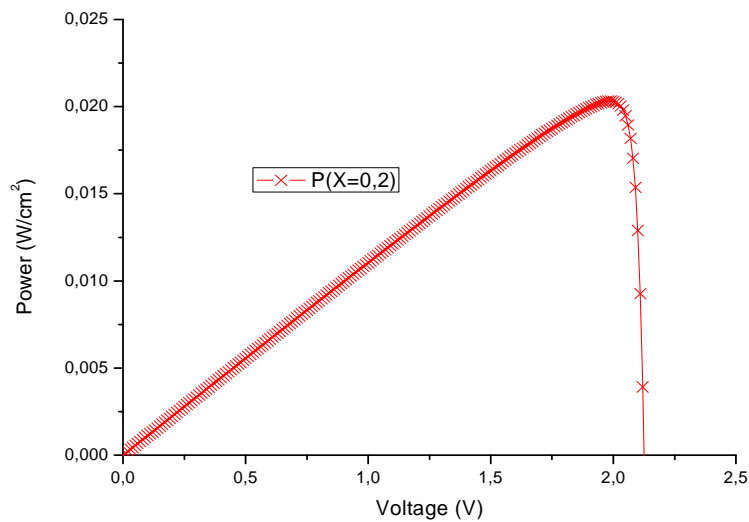


Figure IV.6: The P-V characteristic for x=0.20.

The extracted external parameters of this solar cell from the J-V and the P-V characteristics are presented in table IV.6.

Table IV.6: Parameters of p- InGaN/ n-InGaN solar cell with x=0.20.

J_{sc} (mA/cm ²)	V_{oc} (V)	J_{max} (mA/cm ²)	V_{max} (V)	P_{max} (mW/cm ²)	FF (%)	η (%)
11.19	2.11	10.20	1.99	2.03	85.73	20.31

Chapter IV Results and discussions

We note a significant increase in (J_{sc}) and solar cell efficiency η (The highest value), but a small decrease in V_{oc} .

IV.4.3 Results for proportion of indium $x=0.39$ ($In_{0.39}Ga_{0.61}N$)

The current density-voltage (J-V) characteristic for $x=0.39$ is shown in Figure IV.7.

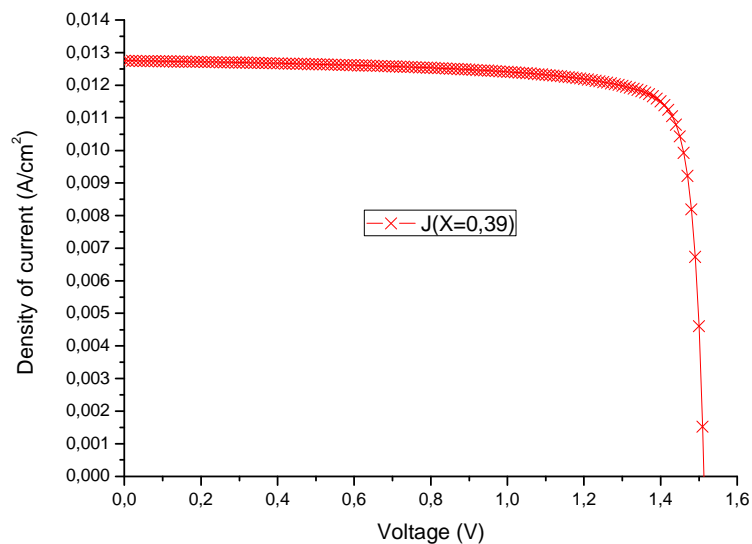


Figure IV.7: The J-V characteristic for $x=0.39$.

The output power-voltage characteristic for the $x=0.39$ is shown in Figure IV.8.

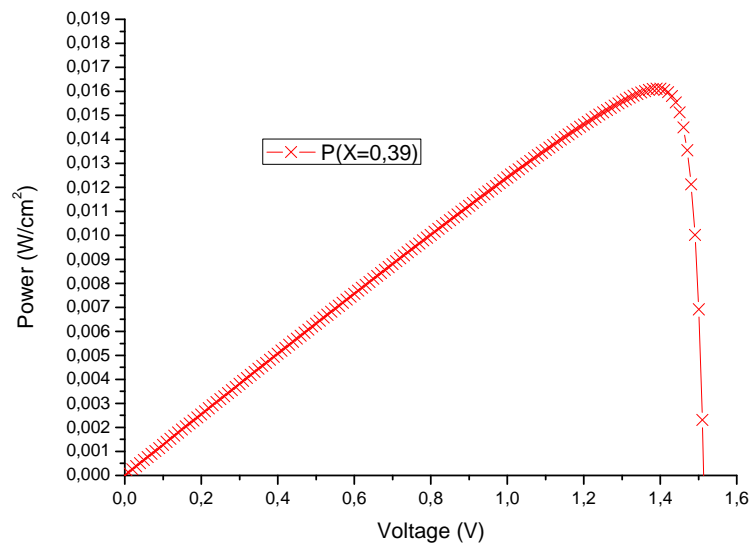


Figure IV.8: The P-V characteristic for $x=0.39$.

The extracted external parameters of this solar cell from the J-V and the P-V characteristics are presented in table IV.7.

Chapter IV Results and discussions

Table IV.7: parameters of p- InGaN/ n-InGaN solar cell with x=0.39.

J_{sc} (mA/cm ²)	V_{oc} (V)	J_{max} (mA/cm ²)	V_{max} (V)	P_{max} (mW/cm ²)	FF (%)	η (%)
12.75	1.52	11.59	1.39	1.61	83.35	16.11

We observe by increasing the percentage of indium(x=0.39) a decrease in all parameters, except density of current(increased less than x=0.2).

IV.4.4 Results for proportion of indium x=0.52 (In_{0.52}Ga_{0.48}N)

The current density-voltage (J-V) characteristic for x=0.52 is shown in Figure IV.9.

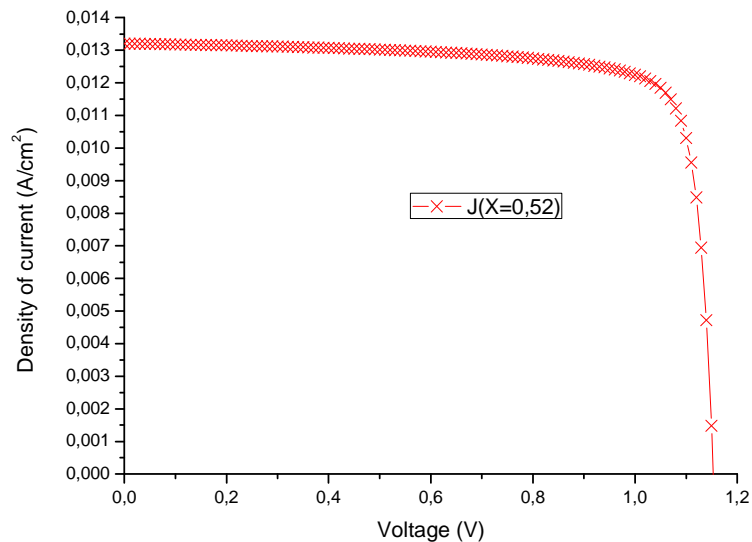


Figure IV.9: The J-V characteristic for x=0.52.

The output power-voltage characteristic for the x=0.52 is shown in Figure IV.10.

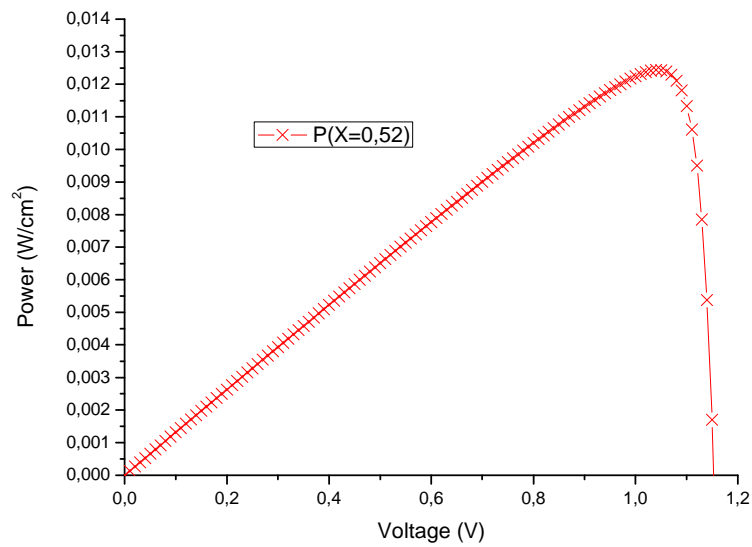


Figure IV.10: The P-V characteristic for $x=0.52$.

The extracted external parameters of this solar cell from the J-V and the P-V characteristics are presented in table IV.8.

Table IV.8: parameters of p- InGaN/ n-InGaN solar cell with $x=0.52$.

J_{sc} (mA/cm ²)	V_{oc} (V)	J_{max} (mA/cm ²)	V_{max} (V)	P_{max} (mW/cm ²)	FF (%)	η (%)
13.2	1.15	11.96	1.03	1.24	81.38	16.11

Also observed that by increasing the percentage of indium; all parameters decrease except J_{sc} .

IV.4.5 Results for proportion of indium $x=0.57$ (In_{0.57}Ga_{0.43}N)

The current density-voltage (J-V) characteristic for $x=0.57$ is shown in Figure IV.11.

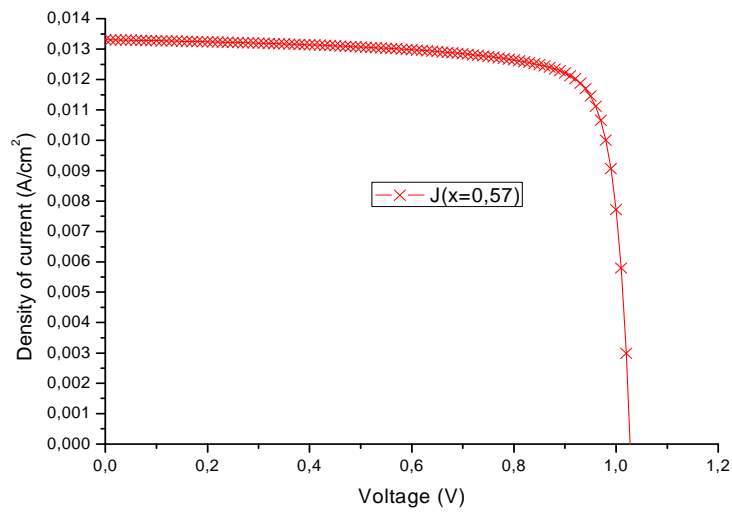


Figure IV.11: The J-V characteristic for $x=0.57$.

The output power-voltage characteristic for the $x=0.57$ is shown in Figure IV.12.

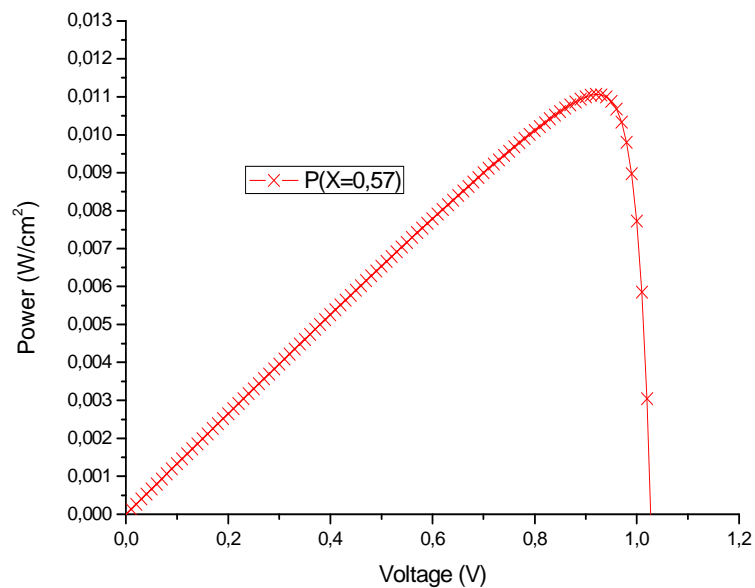


Figure IV.12: The P-V characteristic for $x=0.57$.

The extracted external parameters of this solar cell from the J-V and the P-V characteristics are presented in table IV.9.

Chapter IV Results and discussions

Table IV.9: parameters of p- InGaN/ n-InGaN solar cell with x=0.57.

J_{sc} (mA/cm ²)	V_{oc} (V)	J_{max} (mA/cm ²)	V_{max} (V)	P_{max} (mW/cm ²)	FF (%)	η (%)
13.31	1.02	12.02	0.92	1.10	80.91	11.06

Note at the beginning of this percentage the stability current (Increase is almost non-existent (+0.1 mA)). V_{oc} decreases less than the previous.

IV.4.6 Results for proportion of indium x=0.65 (In_{0.65}Ga_{0.35}N)

The current density-voltage (J-V) characteristic for x=0.65 is shown in Figure IV.13.

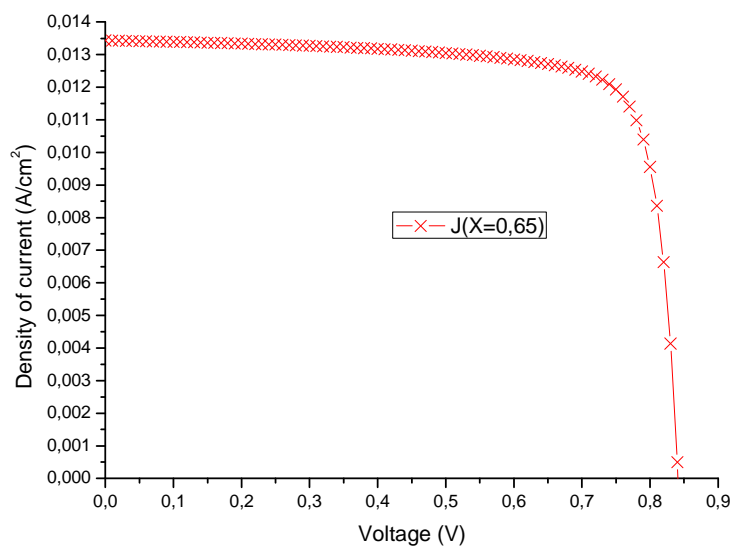


Figure IV.13: The J-V characteristic for x=0.65.

The output power-voltage characteristic for the x=0.65 is shown in Figure IV.14.

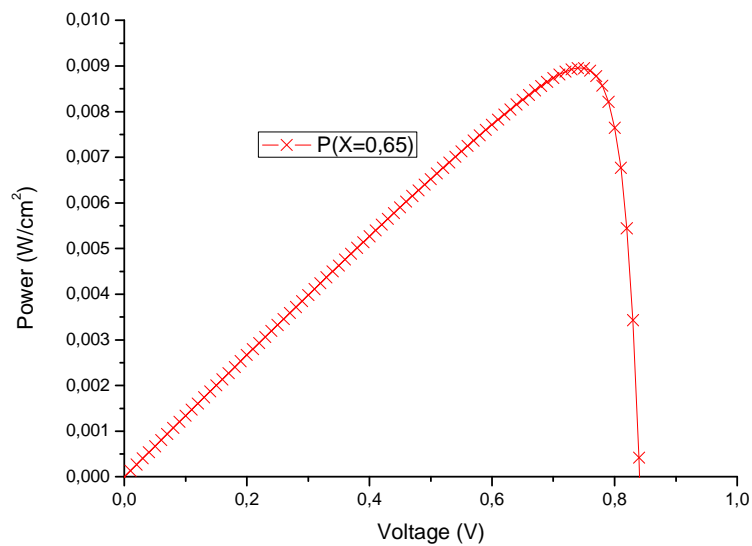


Figure IV.14: The P-V characteristic for $x=0.65$.

The extracted external parameters of this solar cell from the J-V and the P-V characteristics are presented in table IV.10.

Table IV.10: parameters of p- InGaN/ n-InGaN solar cell with $x=0.65$.

J_{sc} (mA/cm ²)	V_{oc} (V)	J_{max} (mA/cm ²)	V_{max} (V)	P_{max} (mW/cm ²)	FF (%)	η (%)
13.43	0.84	12.10	0.73	0.89	79.27	8.95

By more increasing of the percentage of indium; there is no change on the density of short-current (Increase is almost non-existent (+0.1 mA)) but all other parameters have slightly decreased.

IV.4.7 Results for proportion of indium $x=0.68$ ($In_{0.68}Ga_{0.32}N$)

The current density-voltage (J-V) characteristic for $x=0.68$ is shown in Figure IV.15.

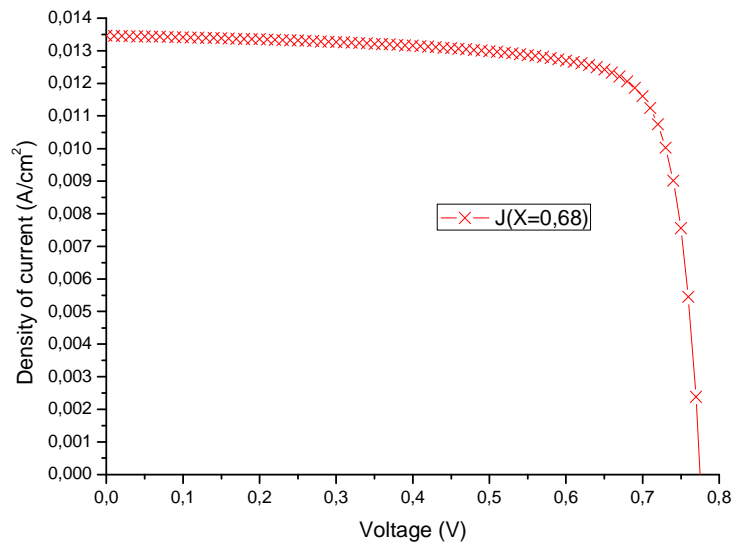


Figure IV.15: The J-V characteristic for $x=0.68$.

The output power-voltage characteristic for the $x=0.68$ is shown in Figure IV.16

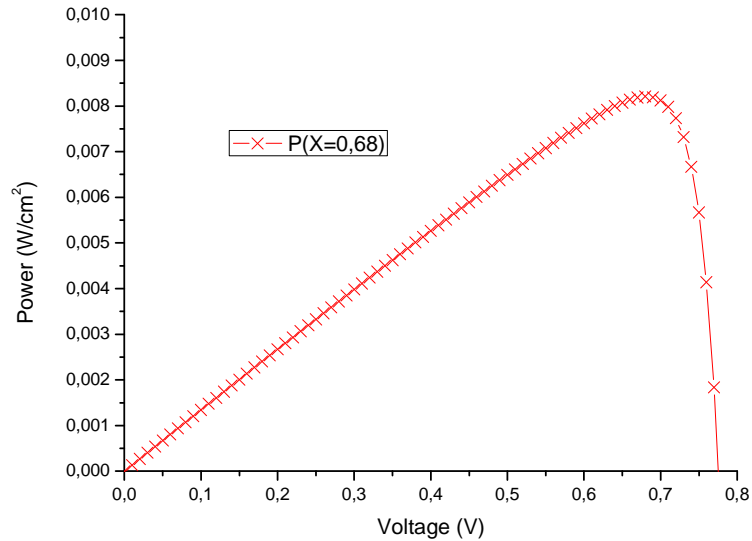


Figure IV.16: The P-V characteristic for $x=0.68$.

The extracted external parameters of this solar cell from the J-V and the P-V characteristics are presented in table IV.11.

Table IV.11: parameters of p- InGaN/ n-InGaN solar cell with $x=0.68$.

Chapter IV Results and discussions

J_{sc} (mA/cm ²)	V_{oc} (V)	J_{max} (mA/cm ²)	V_{max} (V)	P_{max} (mW/cm ²)	FF (%)	η (%)
13.46	0.77	12.06	0.67	0.82	78.25	8.20

Increasing of the percentage of indium estimated by a small amount (0.03); there is also a small change in the density of short-current (Increase) but all other parameters have slightly decreased.

IV.4.8 Results for proportion of indium $x=0.78$ ($In_{0.78}Ga_{0.22}N$)

The current density-voltage (J-V) characteristic for $x=0.78$ is shown in Figure IV.17.

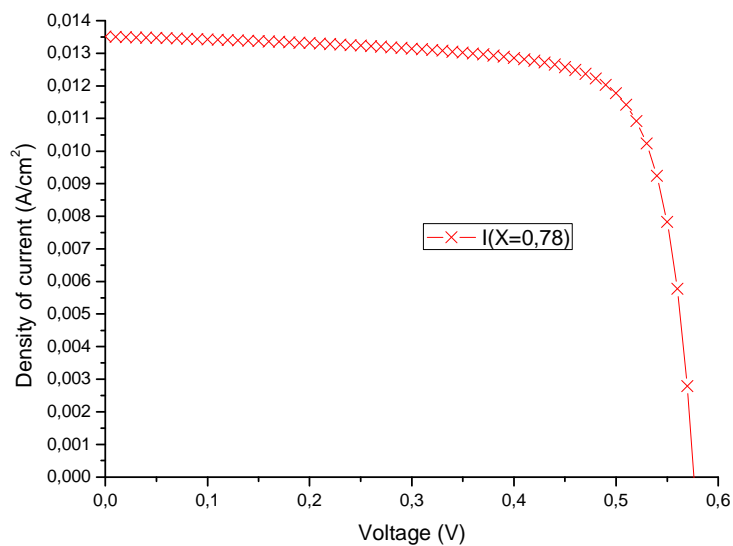


Figure IV.17: The J-V characteristic for $x=0.78$.

The output power-voltage characteristic for the $x=0.78$ is shown in Figure IV.18.

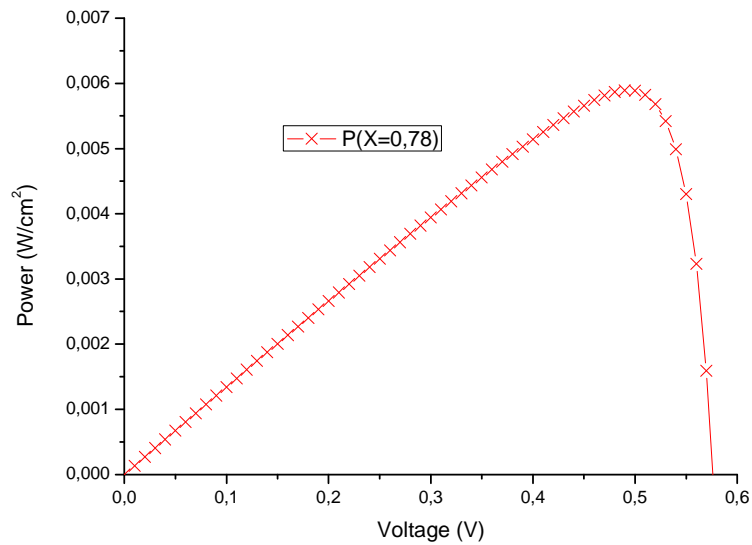


Figure IV.18: The P-V characteristic for $x=0.78$.

The extracted external parameters of this solar cell from the J-V and the P-V characteristics are presented in table IV.12.

Table IV.12: parameters of p- InGaN/ n-InGaN solar cell with $x=0.78$.

J_{sc} (mA/cm ²)	V_{oc} (V)	J_{max} (mA/cm ²)	V_{max} (V)	P_{max} (mW/cm ²)	FF (%)	η (%)
13.51	0.57	12.03	0.48	0.58	75.72	5.89

Increasing of the percentage of indium estimate by a large amount (10%); all parameters decrease except J_{sc} , that is great value ($E_g = 1.1$ eV).

IV.4.9 Results for proportion of indium $x=0.84$ ($In_{0.84}Ga_{0.16}N$)

The current density-voltage (J-V) characteristic for $x=0.84$ is shown in Figure IV.19.

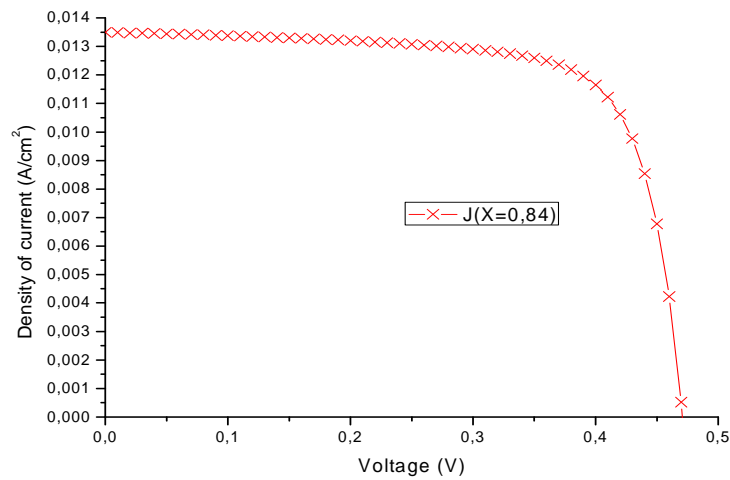


Figure IV.19: The J-V characteristic for x=0.84.

The output power-voltage characteristic for the x=0.84 is shown in Figure IV.20.

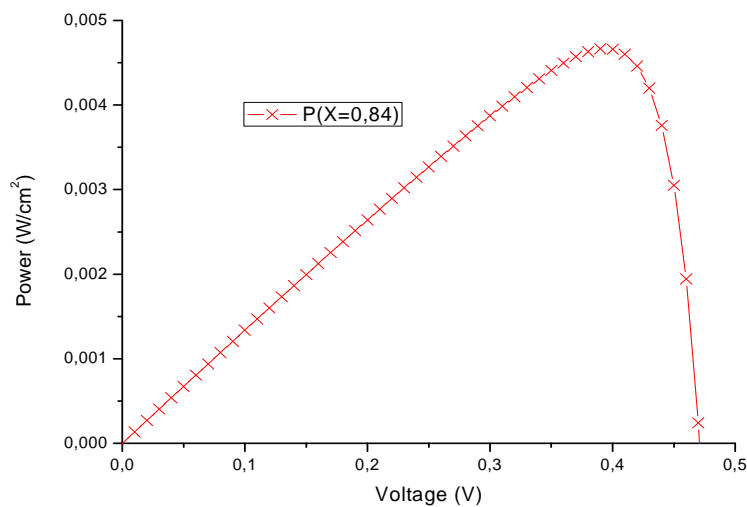


Figure IV.20: The P-V characteristic for x=0.84.

The extracted external parameters of this solar cell from the J-V and the P-V characteristics are presented in table IV.13.

Table IV.13: parameters of p- InGaN/ n-InGaN solar cell with x=0.84.

J_{sc} (mA/cm ²)	V_{oc} (V)	J_{max} (mA/cm ²)	V_{max} (V)	P_{max} (mW/cm ²)	FF (%)	η (%)
13.50	0.46	11.96	0.39	0.46	73.61	4.66

Chapter IV Results and discussions

Increasing of the percentage of indium to alloy; all parameters have slightly decreased.

IV.4.10 Results for proportion of indium $x=0.89$ ($\text{In}_{0.89}\text{Ga}_{0.11}\text{N}$)

The current density-voltage (J-V) characteristic for $x=0.89$ is shown in Figure IV.21.

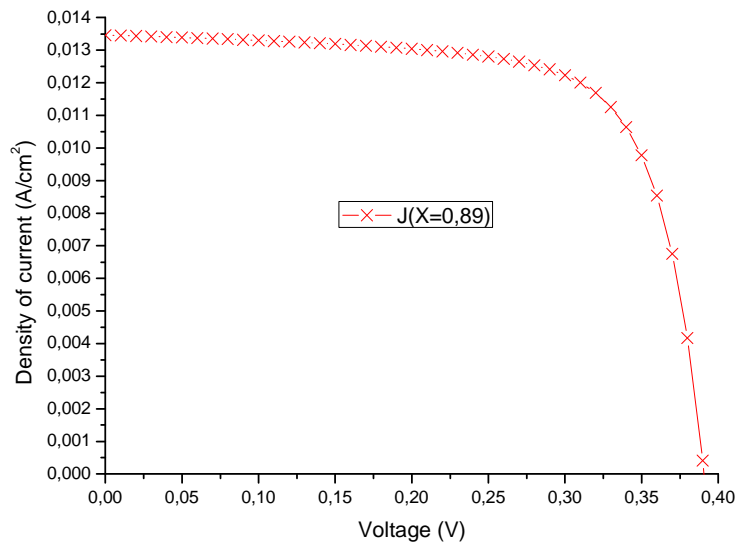


Figure IV.21: The J-V characteristic for $x=0.89$.

The output power-voltage characteristic for the $x=0.89$ is shown in Figure IV.22.

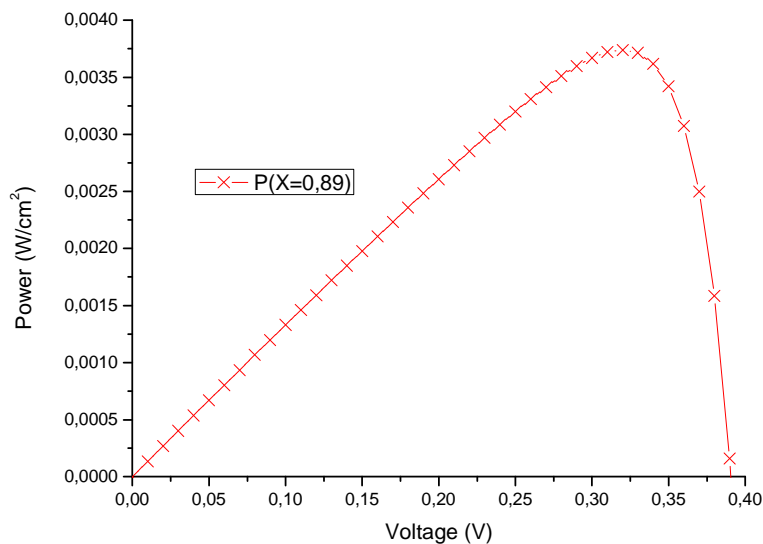


Figure IV.22: The P-V characteristic for $x=0.89$.

Chapter IV Results and discussions

The extracted external parameters of this solar cell from the J-V and the P-V characteristics are presented in table IV.14.

Table IV.14: parameters of p- InGaN/ n-InGaN solar cell with x=0.89.

J_{sc} (mA/cm ²)	V_{oc} (V)	J_{max} (mA/cm ²)	V_{max} (V)	P_{max} (mW/cm ²)	FF (%)	η (%)
13.46	0.39	11.68	0.32	0.37	71.10	4.66

By more increasing of the percentage of indium; all parameters have slightly decreased.

IV.4.11 Results for proportion of indium x=[0-0.89]

The current density-voltage (J-V) characteristic for x= [0-0.89] is shown in Figure IV.23.

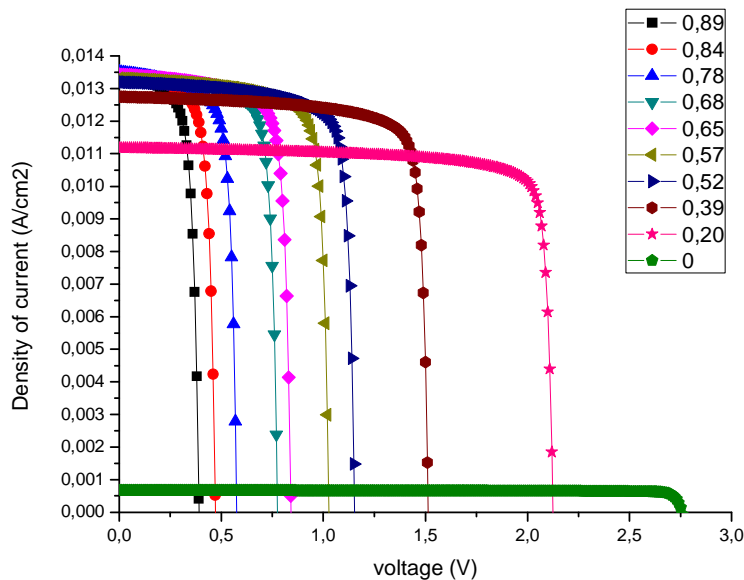


Figure IV.23: The J-V characteristic for different In proportion (x=0→0.89).

This figure all cases presented individually before are assembled together to show the overall effect of the In proportion. When we increase the percentage of indium, there is a rapid increase in the short circuit current density (J) and decrease in open circuit the voltage.

Increasing the proportion of indium (x) decreases the bandgap E_g and thus reduces the absorption of light (or in the absorption coefficient α) (see equation (IV.1.a)), which affects the density of current (increasing) (J) and decrease voltage (V).

IV.5 Summary of indium content in the InGaN (x) absorber layer effect

IV.5.1 The effect on the short circuit current

The effect of the increase of indium (In) content in the InGaN on the short circuit current are summarized in Figure IV.24. It is observed that J_{sc} increases with the increase of x . This is as mentioned before; $x \uparrow \Rightarrow E_g \downarrow \Rightarrow \alpha \uparrow \Rightarrow e-h \text{ pair} \uparrow \Rightarrow J_{sc} \uparrow$.

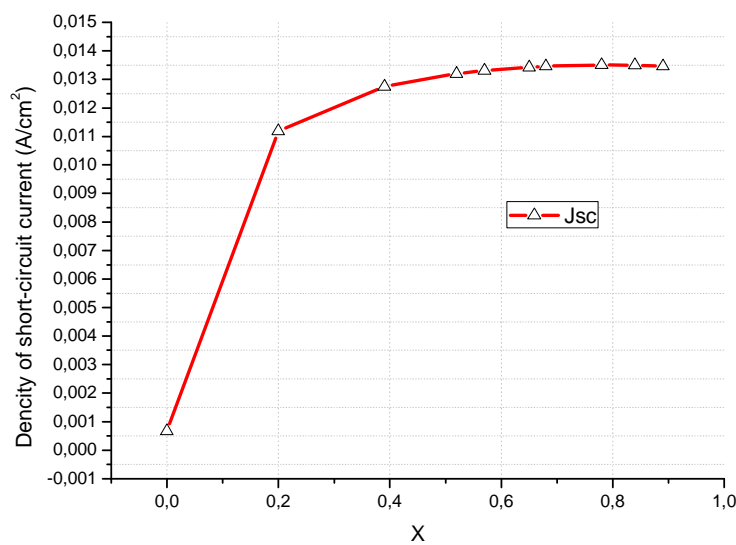


Figure IV.24: Influence of indium content in the InGaN layer on the density of short circuit current of the TCO/p- InGaN/ n-InGaN cell simulated by SILVCO.

IV.5.2 The effect on the open-circuit voltage V_{oc}

The effects of increases of indium (In) content in the InGaN on the open-circuit voltage are summarized in Figure IV.25. It is observed that V_{oc} decreases with the increase of x . This is as mentioned before; $x \uparrow \Rightarrow E_g \downarrow \Rightarrow \alpha \uparrow \Rightarrow e-h \text{ pair} \uparrow \Rightarrow J_{sc} \uparrow \Rightarrow V_{oc} \downarrow$.

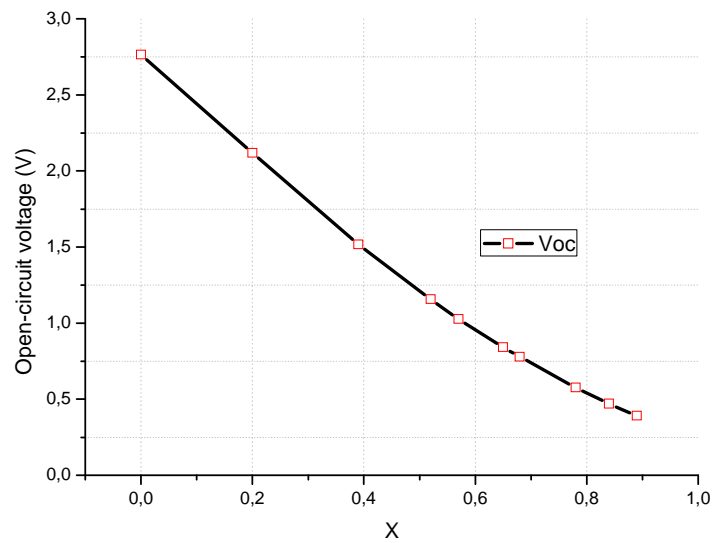


Figure IV.25: Influence of indium content in the InGaN layer on the open-circuit voltage of the TCO/p- InGaN/ n-InGaN cell simulated by SILVCO.

IV.5 .3 The effect on the fill factor (FF)

The effect of increases in indium (In) content in the InGaN on the fill factor is summarized in Figure IV.26. It is observed that Indecreases with in increases x.

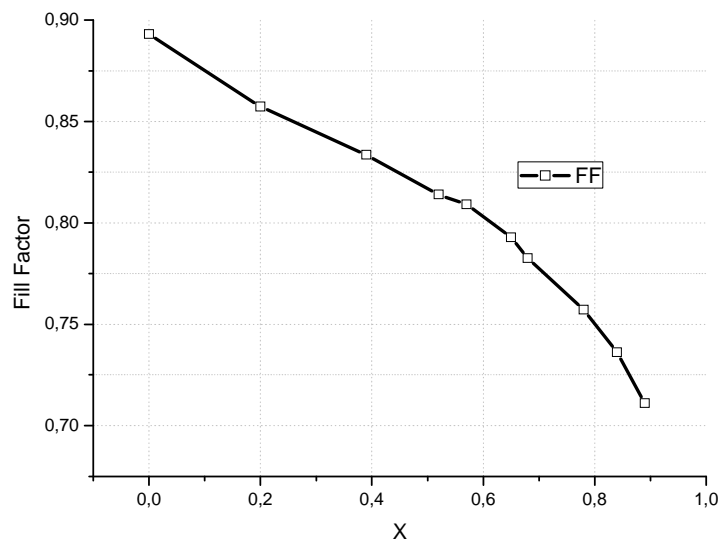


Figure IV.26: Influence of indium content in the InGaN layer on the fill factor of the TCO/p- InGaN/ n-InGaN cell simulated by SILVCO.

IV.5.4 The effect on the efficiency

The effects of increasing the indium (In) content in the InGaN on the efficiency are summarized in Figure IV.27. It is observed that the superlattice when $x=0.2$ ($V_{oc}=2.11$; $J_{sc}=11.19$ mA/cm²). This is because it has the largest power (P_{max}). Compared with (GaN), which has the largest ($v_{oc}=2.76$ V), but J_{sc} very small ($J_{sc}=0.67$ mA/cm²).

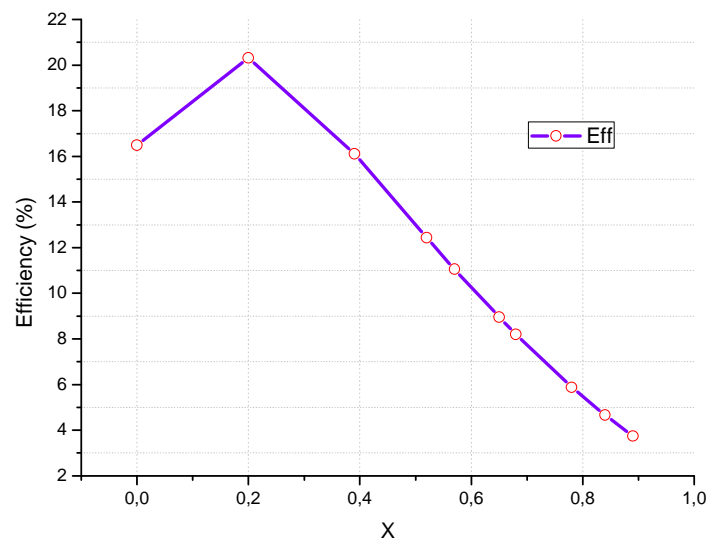


Figure IV.27: Influence of indium content in the InGaN layer on the efficiency of the TCO/p- InGaN/ n-InGaN cell simulated by SILVCO.

IV.6 Comparison between best results of p-n and n-p at $x=0.78$, $In_{0.78}Ga_{0.22}N$

The current density-voltage (J-V) characteristic for p-n $x=0.78$ and n-p $x=0.78$ is shown in Figure IV.28.

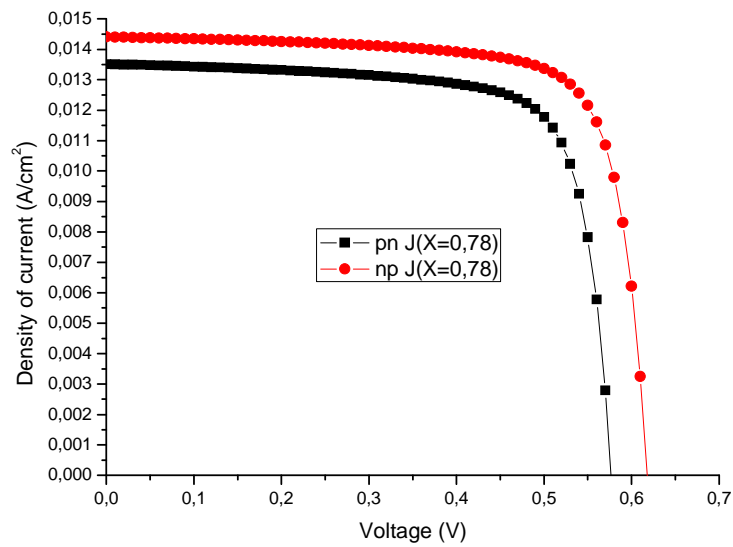


Figure IV.28:The J-V characteristic for a p-n and n-p junction InGaN solar cells for $x=0.78$.

Comparison between best results of p-n and n-p at $X=0.20$, $\text{In}_{20}\text{Ga}_{80}\text{N}$ represented in table IV.15.

Table IV.15: Comparison between a p-n and n-p junction InGaN solar cells for $x=0.78$.

The parameters	p-n junction	n-p junction
Density of short-circuit J_{sc} (mA/cm^2)	13.51	14.40
Open-circuit voltage V_{oc} (V)	0.57	0.61
Fill factor FF	75.72	76.58
Efficiency (%)	5.89	6.80

It is observed that J_{sc} , V_{oc} and η , FF of the n-p junction are better than of the p-n junction.

This is due to the mobility difference; $\mu_n > \mu_h$; (reduce the recombination carriers (e-h)).

General Conclusion

In this work we have studied a p-In_xGa_{1-x}N/n-In_xGa_{1-x}N, homo-junction solar cell. The aim is to study the effect of the Indium proportion on its characteristics (the short current density J_{sc} , the open circuit voltage V_{oc} , the fill factor FF, the efficiency η and the maximum output power P_{MAX}). The proportion of indium for (In_xGa_{1-x}N) was varied from 0 to 0.89. The study was carried out using numerical simulation under the SILVACO software. The In_xGa_{1-x}N layer thickness is fixed in both sides at $W_a=0.01\mu\text{m}$ and $W_d=3\mu\text{m}$ respectively. The doping of the two sides were $N_a=10^{18}\text{cm}^{-3}$ and $N_d=10^{17}\text{cm}^{-3}$ respectively.

For the $x=0$ proportion the short circuit density was quite low (0.67 mA/cm^2) while the open circuit voltage has a large value (2.76 V). A fill factor was around 89.3 which give an efficiency of 16.5%. The adding of 20 % Indium improves the short circuit current significantly to about 11.19 mA/cm^2 . The solar cell efficiency η also improved while a small decrease in V_{oc} was observed (2.11 V).

After that with the increase in the percentage of indium it was noted a slight increase in J_{sc} until up to a saturated value ($J_{sc}=13.51\text{ mA/cm}^2$) when the ratio of Indium is $x=0.78$. The other parameters all decrease. The In_xGa_{1-x}N p-n junction solar cells with different In compositions have been simulated. It is observed that an In_{0.78}Ga_{0.22}N ($E_g = 1.1\text{ eV}$) p-n junction solar cell exhibits the highest density of current 13.51 mA/cm^2 ($V_{oc} = 0.57\text{ V}$ and $\eta = 5.89\%$, $FF = 73.61\%$).

It has to be noted though that the aim is to increase in the short circuit current since this homo-junction solar cell will be used in multi-junction solar cell and in these types of solar cells the short circuit current is the most important parameters.

We have also compared this structure to an n-p structure with the same parameters. It was found that the latter is slightly better. So as a suggestion for further work, is to study the effect of the In proportion of the n-p based solar cell. It is also worth to study the effect of this homo-junction solar cell in the multi-junction solar cell. It may be also interesting to study a hetero-junction solar cell to find if there is any improvement.

References

REFERENCES

- [1] X. Zhang, X. Wang, H. Xiao et al., "Simulation of In_{0.65}Ga_{0.35}N single-junction solar cell," *Journal of Physics D*, vol. 40, no. 23, pp. 7335–7338, (2007).
- [2] O. Jani, C. Honsberg, A. Asghar et al., "Characterization and analysis of InGaN photovoltaic devices," in *Proceedings of the 31st IEEE Photovoltaic Specialists Conference*, pp. 37–42, Lake Buena Vista, Fla, USA, (January 2005).
- [3] H. Hamzaoui, A. S. Bouazzi, and B. Rezig, "Theoretical possibilities of In_xGa_{1-x}N tandem PV structures," *Solar Energy Materials and Solar Cells*, vol. 87, no. 1–4, pp. 595–603, (2005).
- [4] J. F. Muth, J. H. Lee, I. K. Shmagin et al., "Absorption coefficient, energy gap, exciton binding energy, and recombination lifetime of GaN obtained from transmission measurements," *Applied Physics Letters*, vol. 71, no. 18, pp. 2572–2574, (1997).
- [5] J. Wu, W. Walukiewicz, K. M. Yu et al., "Superior radiation resistance of In_{1-x}Ga_xN alloys: full-solar-spectrum photovoltaic material system," *Journal of Applied Physics*, vol. 94, no. 10, pp. 6477–6482, (2003).
- [6] M. Ueno, M. Yoshida, A. Onodera, O. Shimomura, and K. Takemura, *Phys. Rev. B* 49,14 (1994).
- [7] W. C. Johnson, J. B. Parsons, and M. C. Crew, *J. Phys. Chem.* 36, 2561 (1932).
- [8] A. Berger, D. Troost, and W. Mönch, *Vacuum* 41,669 (1990).
- [9] J. E. Andrews and M. A. Littlejohn, *1. Electrochem. Soc.* 122, 1273 (1975).
- [10] M. Furtado and G. Jacob, *J. Cryst. Growth* 64, 257 (1983).
- [11] A. Addamiano, *J. Electrochem. Soc.* 108, 1072 (1961).
- [12] Z. A. Munir and A. W. Searcy, *J. Chem. Phys.* 42, 4223 (1965).
- [13] V. Y. Michailin, Y. E. Oranovskii, S. Pacesova, J. Pastrnak, and A. S. Salamatov, *Phys. Status Solidi B* 55, K51 (1973).
- [14] S. Nakamura, *Jpn. J. Appl. Phys.* 30, L1705 (1991).
- [15] M. Ilegems and H. C. Montgomery, *Chern. Solids, J. Phys* 34, 885 (1973).
- [16] H. P. Maruska and J. J. Tietjen, *Appl. Phys. Lett.* 15, 327 (1969).
- [17] B. Monemar, *Phys. Rev. B* 10, 676 (1974).
- [18] J.I.Pankove, H.P. Maruska, and I. E. Berkeyheiser, *Appl. Phys. Lett.* 17,197(1970).
- [19] K. T. McCarron, G. R. Kline, J. T. Martin, and K. M. Lakin, *Proc. IEEE Ultrasonics Symp.* 3, 673 (1988).
- [20] E. Ejder, *Phys. Status Solidi A* 6, 445 (1971).

References

- [21] E. D. Palik, Handbook of Optical Constants of Solids, Academic, New York (1985).
- [22] M. J. Ilegems, Cryst. Growth 13/14, 360 (1972).
- [23] G. Bums, F. Dacol, J. C. Marinace, B. A. Scott, and E. Burstein, Appl. Phys. Lett. 22, 356 (1973).
- [24] D. K. Wickenden, K. R. Faulkner, R. W. Brander, and B. J. Isherwood, Cryst. Growth 9, 158 (1971).
- [25] J. I. Pankove, H. P. Maruska, and J. E. Berkeyheiser, Appl. Phys. Lett. 17, 197 (1970).
- [26] E. K. Sichel and J. I. Pankove, J. Phys. Chem. Solids, 38, 330 (1977).
- [27] A. S. Barker and M. Ilegems, Phys. Rev. B 7, 743 (1973).
- [28] I. Akasaki, H. Amano, M. Kito, and K. Hiramatsu, J. Lumin. 48/49, 666 (1991); H. Amano, M. Kito, K. Hiramatsu, and I. Akasaki, Inst. Phys. Conf. Ser. 106, 725 (1990).
- [29] S. Nakamura, T. Mukai, and M. Senoh, *ibid.* 30, L1998 (1991).
- [30] p. Bergman, G. Ying, B. Monemar, and P. O. Holtz, J. Appl. Phys. 61, 4589 (1987).
- [31] M. Ilegems, R. Dingle, and R. A. Logan, J. Appl. Phys. 43, 3797 (1972).
- [32] J. I. Pankove and J. A. Hutchby, J. Appl. Phys. 47, 5387 (1976).
- [33] E. Ejder and H. G. Grimmeiss, J. Appl. Phys. 5, 275 (1974).
- [34] R. D. Cunningham, R. W. Brander, N. D. Knee, and D. K. Wickenden, J. Lumin. 5, 21 (1972).
- [35] J. I. Pankove, M. T. Duffy, E. A. Miller, and J. E. Berkeyheiser, J. Lumin. 8, 89 (1973).
- [36] V. S. Ban. Mass spectrometric and thermodynamic studies of the CVD of some III-V compounds. Journal of Crystal Growth, 17, 19–30, (1972).
- [37] J. Schmid, Photovoltaik: ein Leitfadens für die Praxis; ein Informationspaket; Köln: Verl. TÜV Rheinland, pg. 10-12. (1995).
- [38] Umamaheswari Balasubramanian, Master's Thesis, Electrical Engineering, University of South Florida, (2004).
- [39] F. A. Lindholm, J. G. Fossum, E. L. Burgess, Application of the Superposition Principle to solar-cell Analysis. IEEE Transactions on Electron Devices. 26:165–171. (1979).
- [40] R. Pierret, Semiconductor Device Fundamentals, Chap. 2, Addison-Wesley, Reading, MA, 23–74 (1996).
- [41] Atlas User's Manual, 2-2, (2004).
- [42] Atlas User's Manual, 1-2, (2004).
- [43] Atlas User's Manual, 2-8, (2004).

References

- [44] A. D. Bates, "Novel optimization techniques for multijunction solar cell design using Silvaco Atlas", Master's Thesis, Naval Postgraduate School, Monterey, California, 19, (2004).
- [45] A. D. Bates, "Novel optimization techniques for multijunction solar cell design using Silvaco Atlas", Master's Thesis, Naval Postgraduate School, Monterey, California, 20, (2004).
- [46] A. D. Bates, "Novel optimization techniques for multijunction solar cell design using Silvaco Atlas", Master's Thesis, Naval Postgraduate School, Monterey, California, 21, (2004).
- [47] G.F. Brown, J. W. Ager, W. Walukiewicz and J. Wu, Finite element simulations of compositionally graded InGaN solar cells, *Solar Energy Mater. Solar Cells* 94:478–83, (2010).
- [48] J. F. Muth, J. H. Lee, I. K. Shmagin, R. M. Kolbas, H. C. Casey, B. P. Keller, U. K. Mishra and DenBaars, S. P. Absorption coefficient, energy gap, exciton binding energy, and recombination lifetime of GaN obtained from transmission measurements, *Appl. Phys. Lett.* 71:2572–4, (1997).
- [49] J. Wu and W. Walukiewicz, Band gaps of InN and group III nitride alloys, *Superlattices Microstruct.* 34:63–75, (2003).
- [50] M. Farahmand, C. Garetto, E. Bellotti, K. F. Brennan, M. Goano, E. Ghillino, G. Ghione, J. D. Albrecht and P. P. Ruden, Monte Carlo simulation of electron transport in the III-nitride Wurtzite phase materials system: Binaries and Ternaries, *IEEE Trans. Electron Devices* 48:535–42, (2001).
- [51] M. E. Levinstein, S. L. Rumyantsev, and M. S. Shur, *Properties of Advanced Semiconductor Materials*, John Wiley & Sons, New York, NY, USA, (2001).
- [52] P. D. C. King, Veal T. D., Kendrick C. E., Bailey L. R., Durbin S. Mand McConville C. F., InN/GaN valence band offset: High-resolution x-ray photoemission spectroscopy measurements, *Phys. Rev. B* 78:033308, (2008).
- [53] K. A. Wang, C. Lian, N. Su and D. Jena, Conduction band offset at the InN/GaN heterojunction, *Appl. Phys. Lett.* 91:232117, (2007).
- [54] S. Adachi, *Handbook on the properties of semiconductors, Volume 2: 111-V Compound Semiconductors*, Kluwer Academic Publishers, London, (2004).